ION-INDUCED MODIFICATIONS IN GALLIUM PHOSPHIDE SINGLE CRYSTALS

BY

ZAMZAM IBNU SINA

A Thesis Presented to the

DEANSHIP OF GRADUATE STUDIES

KING FAHD UNIVERSITY OF PETROLEUM & MINERALS

DHAHRAN, SAUDI ARABIA

In Partial Fulfillment of the
Requirements for the Degree of

MASTER OF SCIENCE

In

PHYSICS

APRIL 2018

KING FAHD UNIVERSITY OF PETROLEUM & MINERALS

DHAHRAN- 31261, SAUDI ARABIA

DEANSHIP OF GRADUATE STUDIES

This thesis, written by **Zamzam Ibnu Sina** under the direction of his thesis advisor and approved by his thesis committee, has been presented and accepted by the Dean of Graduate Studies, in partial fulfillment of the requirements for the degree of **MASTER OF SCIENCE IN PHYSICS.**

Dr. Abdullah A. AlSunaidi
Department Chairman

Dr. Ayman Sherif El-Said
(Advisor)

Dr. Salam A. Zummo
Dean of Graduate Studies

Dr. Hocine Bahlouli
(Member)

10/5/18
Date

Dr. Abdelkarim Mekki
(Member)

Dedicated to my parents

ACKNOWLEDGMENTS

All thanks and praise belong to Allah ta'aala for the innumerable gifts and bounties showered upon us daily. In addition, I convey my deepest gratitude to my thesis advisor Dr. Ayman El-Said for his extensive encouragement, guidance, support, ideas and assistance with troubleshooting throughout the course of this research project. Also, I am grateful to my thesis committee members: Dr. Abdelkarim Mekki, for his support, encouragement, time and assistance towards a successful thesis, and Dr. Hocine Bahlouli, for his words of encouragement during the course of my work. Furthermore, I convey my sincerest thanks to the entire physics faculty and staff members for their innumerable instances of support, whether direct or indirect, during my research efforts.

In particular, I would like to pay special gratitude to those professors who are also my teachers: Dr. M. M. Faiz, Dr. F. Z. Khiari, Dr. T. A. Al-Aithan, Dr. I. M. A. Nasser, Dr. M. F. Al-Kuhaili, Dr Khalil Ziq, Dr. Saleem Rao, Dr. A. A. Naqvi and Dr. Khalil Harrabi. Also, to the chairman of the physics department, Dr. A. A. Al-Sunaidi, I utter my heartfelt thanks for his endless support in all our endeavours. I am thankful to the following persons: Mr. M. Hassan Al-Saeed, Mr. Abul Lais, Mr Lutfi Mulyadi, Mr Muhammad Hanif, and all member of Indonesian community in KFUPM; I thank you all.

Also, I thank the Deanship of Scientific Research for financial aid during the course of this work. Above all, sincere acknowledgment is due to the Kingdom of Saudi Arabia and King Fahd University of Petroleum and Minerals (KFUPM) for offering this amazing scholarship. Lastly, I am always grateful to my parents, my brother, and my wife for their constant support and care in countless forms till date.

TABLE OF CONTENTS

LIST OF TABLES

LIST OF FIGURES

LIST OF ABBREVIATIONS

AFM	:	Atomic Force Microscopy
EBIT	:	Electron Beam Ion Trap
GaP	:	Gallium Phosphide
HCI	:	Highly Charged Ions
RBS	:	Rutherford Backscattering Spectrometry
SHI	:	Swift Heavy Ions
UNILAC	:	Universal Linear Accelerator
XPS	:	X-ray Photoelectron Spectroscopy

ABSTRACT

Full Name : Zamzam Ibnu Sina

Thesis Title : Ion-Induced Modification in Gallium Phosphide Single Crystals

Major Field : Physics

Date of Degree : April 2018

Ion beam techniques have been utilized successfully to modify both the surface and bulk properties of various solids. The ion-induced effect depends mainly on the ion and material properties. Here, we are focusing on studying one of the promising semiconductors, namely gallium phosphide (GaP) single crystals, after irradiation with slow highly charged ions (HCI) and swift heavy ions (SHI). The ion-irradiation was performed using different ion species of different kinetic energies and carrying various charge states. For HCI, the samples were irradiated with various charge state of Xe^{q+} ions (q=33-40) exhibiting kinetic energy of 114 keV. For SHI, the samples were irradiated with I ions of 1-54 MeV and Au ions of 240 MeV-1.16 GeV with ion fluence varying from 5×10^9 to 1×10^{14} ions cm^{-2}. The ion-induced modifications in GaP samples were investigated by means of atomic force microscopy (AFM), Rutherford backscattering spectrometry (RBS), X-ray photoelectron spectroscopy, and UV-Vis spectroscopy. Based on the AFM measurements, the irradiation of GaP single crystals using HCI showed no observable change of the surface topography, whereas nanohillocks were observed after irradiation with SHI. Significant damage of the GaP crystal was observed using RBS after irradiation with 1 MeV I of high fluence. Amorphization was even observed for the samples irradiated with 1 MeV I at fluence 1×10^{14} ions cm^{-2}. Amorphization was not observed for the samples irradiated with 54 MeV I and 1.16 GeV Au implying that amorphization is most likely induced by nuclear energy

deposition via elastic collisions of ions with the target atoms. Moreover, transmission spectra of the SHI irradiated samples revealed red shift of the absorption edge in comparison to the one observed for the virgin sample indicating a reduction of the band gap. The band gap was found to be decreasing as a function of ion fluence and ion energy loss, which is ascribed to the formation of localized states into the forbidden energy band. The results of the performed experiments are expected to contribute highly in reaching better understanding of the damage creation mechanism and control of the modifications induced by HCI and SHI in semiconductors.

ملخص الرسالة

الاسم الكامل : زمزم ابن سينا

عنوان الرسالة : دراسة تأثير الأيونات على بلورات فوسفيد الجاليوم الأحادية

التخصص : الفيزياء

تاريخ الدرجة العلمية : أبريل 2018

هذة الرسالة تهدف إلى دراسة تأثير الأيونات على بلورات فوسفيد الجاليوم الأحادية وذلك بتشعيعها بأيونات بطيئة عالية الشحنة و الأخرى السريعة عالية الطاقة .استخدمت في هدة التجارب أيونات متنوعة ذات طاقات حركة مختلفة وحاملة لشحنات مختلفة . تم دراسة امكانية بناء اشكال نانوميترية عن طريق قياسات ميكروسكوبية فى المدى النانوميترى باستخدام جهاز SFM . و حيث أن السبب الرئيسى المبدئى لتكون الأشكال النانوميترية باستخدام كلا من الأيونات البطيئة عالية الشحنة والأخرى السريعة عالية الطاقة هوا اللإثارة اللإلكترونية العالية فإن مقارنة كلا من التقنيتين كانت من الأهمية بمكان لفهم عملية التكوين للأشكال النانوميترية في هذة المادة .إضافا" إلى استخدام طرق الطيف الضوئى و XPS لمعرفة التغيرات السطحية بعد التشعيع بأيونات سريعة عالية الطاقة. :

تم أيضا دراسة التغيرات داخل المادة باستخدام تقنيتين: الأولى هى UV-Vis Spectroscopyوهذا لدراسة الخصائص الضوئية للمادة. التقنية الثانية هى RBSحيث تم دراسة التغيرات في التركيب البلوري للمادة بعد التشعيع. و قد اظهرت النتائج ان التشعيع بالأيونات عالية الطاقة كان لة قدرة فائقة لعمل تغييرات في هذة المادة والتي تتبع أشباه الموصلات . ومن النتائج الواعدة والمهمة تكنولوجيا انه يمكن التحكم في فجوة الفرقة band gap بتغيير كلا من طاقة الحركة المرسبة و الجرعة الاشعاعية للأيونات المستخدمة. هذا أضافا الى ملاحظة تغير ملحوظ في التركيب البلوري لمادة فوسفيد الجاليوم وصل الى حد التحول للحالة الامورفية بعد التشعيع بأيونات اليود عالية الطاقة وبجرعة اشعاعية عالية .

CHAPTER 1

INTRODUCTION

1.1 Motivation

During the past 50 years ion beam technology has demonstrated its effectiveness and uniqueness in the continuously growing field of material science and engineering. It covers wide range of applications such as analysis e.g. elastic recoil detection analysis (ERDA) and Rutherford backscattering spectrometry (RBS), synthesis of nanocomposite, and modification of materials properties. They have been versatile tools due to their numerous controllable parameters such as ion kinetic energy (eV-GeV), ion species, ion fluence, and ion charge state [1].

The specific application of ion beams requires a detailed knowledge of the interactions of the energetic ions with the target material. These interactions dictate the primary energy deposition leading to structural modifications induced in the material (radiation damage) and the depth at which the ions come to rest. In addition, the radiation damage induced by ion irradiation depends on the external irradiation conditions and the properties of the material under investigation.

Ion beams have been widely used for tailoring the desired properties in materials to fit their applications in various fields. For instance, irradiation of various materials with swift heavy ions (SHI) of MeV-GeV kinetic energy range can lead to permanent structural

modifications not only in solid surfaces, e.g. creation of hillock- or crater-type nanostructures but also in the bulk, e.g. ion track formation [2–4]. This enabled new applications as for instance the controlled shaping of embedded nanoparticles, which could not be imagined beforehand. Moreover, SHI irradiation with sufficiently high ion fluence leads to track overlapping and formation of extended amorphous layers [5, 6].

Ion beams also played an important role in other fields such as treatment of radioactive waste in nuclear fission and fusion technologies, space craft protection from the exposure to cosmic radiation, and the treatment of cancer using ion beam [7, 8].

A significant advantage of SHI irradiation in surface nanostructuring is that the structures are created without chemical treatment as used in conventional optical lithographic methods. Recently, it has also been reported that irradiation with slow highly charged ions (HCI) can lead to similar surface modifications without damaging the bulk due to the high potential energy deposition within a nanometer size volume close to the surface [9–11]. This makes slow highly charged ions a suitable and gentle tool for surface nanostructuring, cleaning, and modifications of different materials.

The recent previous work in this field of interest showed that the highly energetic heavy ions were able to produce optical modifications in various materials such as Si [12], InP [13], CdO [14], SnO2 [15], MoO3 [16], SiC [17], and various types of polymer [18, 19]. This particular modification can be very useful in manufacturing semiconductors material considering their common applications in electronic and optical devices.

The ion-matter interaction is well understood in insulating materials as well as in some intermetallic compounds and metals. However, the behaviour of semiconductors under ion-

irradiation appears to be different from that of metals or insulators [20]. In comparison to insulators and metals, semiconductors were less studied regarding creation of damage induced by ion-irradiation. The understanding of defect creation mechanisms after ion-irradiation in semiconductors is of high importance for many applications e.g. in the fabrication of electronic devices.

In this work, several single crystals of gallium phosphide (GaP) will be studied using different techniques after irradiation with both SHI and HCI. The comparison between the effects induced by these two different types of ions is aiming to reach a better understanding of the ion-induced damage in semiconductors.

1.2 Aim of Work

This thesis is mainly devoted to study the modifications induced by both slow highly charged ions (HCI) and swift heavy ions (SHI) in gallium phosphide (GaP) single crystals. The results from the performed experiments are expected to contribute highly for reaching better understanding of the creation mechanism and control of the modifications induced by HCI and SHI in semiconductors.

1.3 Thesis Structure

The fundamentals of ion–solid interaction, theoretical description of ion track formation and ion-induced modification in a broad variety of materials have been subject of intensive studies. Literature review of previous results are discussed and presented in Chapter 2.

Chapter 3 provides a brief introduction about gallium phosphide (GaP), which is the used material in this study. In addition, description of the ion-irradiation facilities are introduced. Moreover, various techniques were used to characterize the GaP samples such as Atomic Force Microscopy (AFM), Rutherford Backscattering Spectrometry (RBS), X-ray Photoelectron Spectroscopy (XPS), and UV-vis spectroscopy. Complete description of these techniques including the principles and experimental details are also given in this chapter.

All experimental results and discussions are presented in Chapter 4. AFM measurements were performed to investigate the surface morphology of the samples. RBS measurements were carried out to determine the composition and probe the structural change in the GaP single crystal induced by ion-irradiation. The structural modifications induced by ion-irradiation in the GaP surface were studied using XPS. Furthermore, UV-vis spectroscopy was applied extensively to study the changes in the optical properties induced by ion bombardment.

Finally, the most important results are summarized in the Conclusions.

CHAPTER 2

Theoretical Background

2.1 Ion-Solid Interaction

2.1.1 Nuclear and Electronic Energy Loss

When material is irradiated with ions, the ions move through the material changing continuously their direction and energy and maybe also their states of excitation and ionization. Finally, the ions come to rest within the target (implanted) or they leave the target (transmitted or backscattered). Along its trajectory through the material, the ion loses its energy predominantly due to elastic collision with nuclei which is referred to as nuclear energy loss $\left(\frac{dE}{dx}\right)_n$ and inelastic collision with electrons which is referred to as electronic energy loss $\left(\frac{dE}{dx}\right)_e$. Hence, the total energy loss can be written as

$$\left(\frac{dE}{dx}\right) = \left(\frac{dE}{dx}\right)_n + \left(\frac{dE}{dx}\right)_e \qquad (1)$$

For slow heavy ions (of mass number $M > 4$) typically with energy below 10 keV/u, ion energy loss is mainly due to elastic collision with the nuclei [1]. This collision could generate secondary recoils and collision cascade. Therefore, target atoms can become displaced producing point defects and extended defects. The displaced atoms can be removed from the surface creating what is called nuclear sputtering. Hence, nuclear energy loss yields lattice defect by displacement of atoms from their original positions.

In the case of swift heavy ions exhibiting kinetic energy typically above 100 keV/u, the electronic energy loss is the dominating energy transfer mechanism. The transfer of energy to electrons leads to either excitation where the electron is excited to the higher states or ionization where the electron is ejected from the atom. The damage in the lattice e.g. ion tracks and more extended defect structures e.g. voids can be generated. These defects are caused by electronic energy loss through the electron-phonon interaction. Many works have shown that the radii of molten damaged zone is proportional to the electronic energy loss [6, 21, 22]. Moreover, SHI irradiation with sufficiently high ion fluence leads to track overlapping and formation of extended amorphous layers [5].

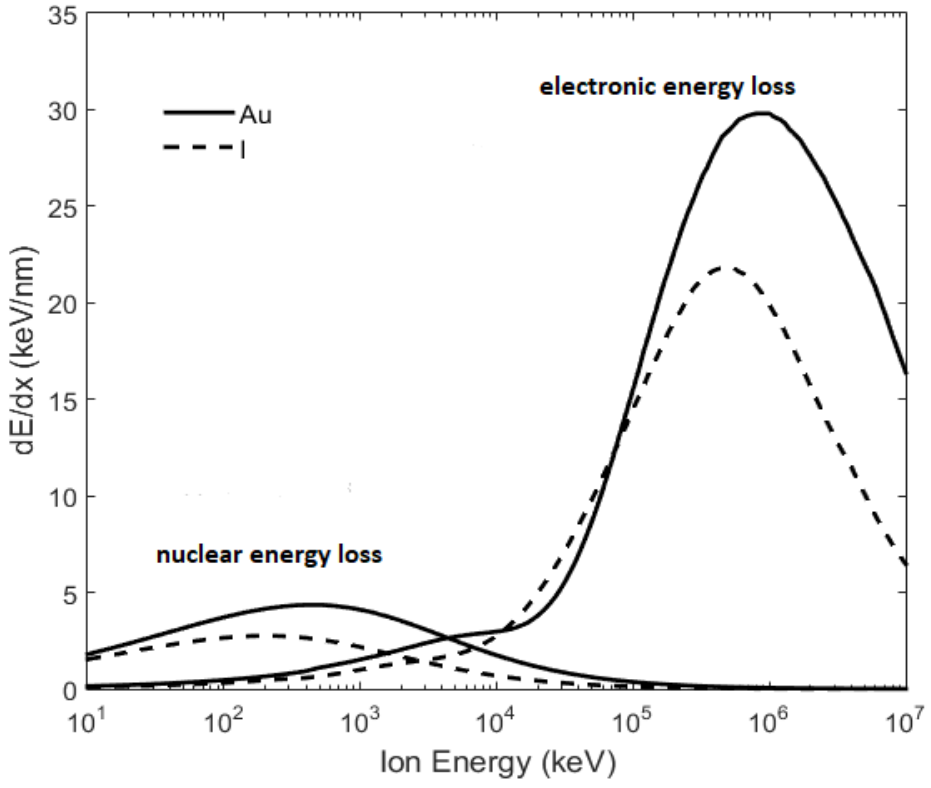

Figure 1. Energy loss of gold and iodine ions in GaP, calculated using the SRIM-2013 [23].

Both $\left(\frac{dE}{dx}\right)_n$ and $\left(\frac{dE}{dx}\right)_e$ increase as a function of the kinetic energy of the ion until it reaches the maximum value and then decreases (Figure. 1). The maximum point for electronic

energy loss is known as Bragg's peak. The value of electronic energy loss is proportional to the square root of ion velocity $E^{1/2}$ This approximation is reasonable when the ion velocity is less than the (orbital) velocity of electrons [24]. Whereas in the region above Bragg's peak, the electronic energy loss is proportional to $1/E$. The approximation for the electronic energy loss is given by Bethe-Bloch formula [25]

$$\frac{dE}{dx} = \frac{4\pi e^4 Z_{eff}^2 Z_t N}{m v_{ion}^{\ 2}} \left\{ \ln\left(\frac{2mc^2\beta^2}{I} \right) - \beta^2 - \delta - U \right\} \tag{2}$$

$e =$ electronic charge

$Z_{eff} =$ effective charge of the ions in the materials

$Z_t =$ nuclear charge of the target atoms

$N =$ number of target atoms per unit volume

$m =$ mass of electron

$\beta =$ speed of ion in unit of speed of light c

$I =$ mean ionization potential of the target atoms

$\delta =$ correction factor for polarization effect

$U =$ low velocity correction

Using TRIM-2013 software, we can simulate the trajectory of the ions inside the material as shown in Figure 2. There is a distinct difference between the damage produced by the nuclear and electronic energy loss. Nuclear collisions result in the deviation of the projectile direction. Therefore, ions with dominant nuclear energy loss follow a zigzag motion until they come to rest. This leads to a spatially extended damage distribution due to the elastic collisions of ion with the nuclei and the collision cascades. On the other hand, ions with dominant electronic energy loss, move in a straight line.

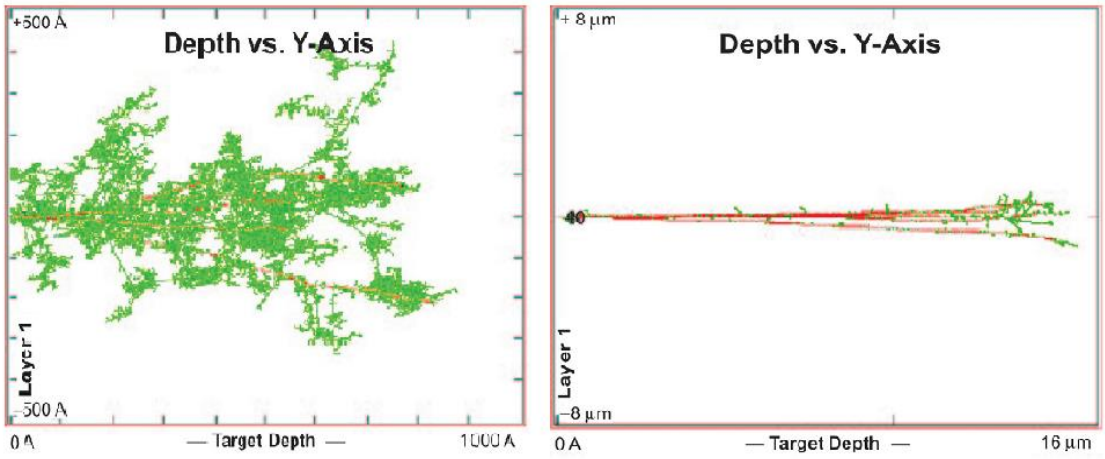

Figure 2. Comparison of ion trajectory (red) produced by 100 keV ions (left) and 1 MeV ions (right) obtained using TRIM simulation software [23]**. The green color represents trajectory of the secondary recoils.**

2.1.2 Ion Range

Ion range is defined as the integrated distance that an ion travels inside the material until it stops. By knowing the total energy loss, we can also calculate the total range of ions in material using integration as follow

$$S = -\frac{dE}{dx} \tag{3}$$

$$R = \int_0^{E_{in}} \frac{dE}{S} \tag{4}$$

where E_{in} is the initial kinetic energy of the ions.

Figure 3 shows the travelled distance of energetic ion inside material explaining the difference between ion range R, projected range R_p, and penetration depth X_s [26].

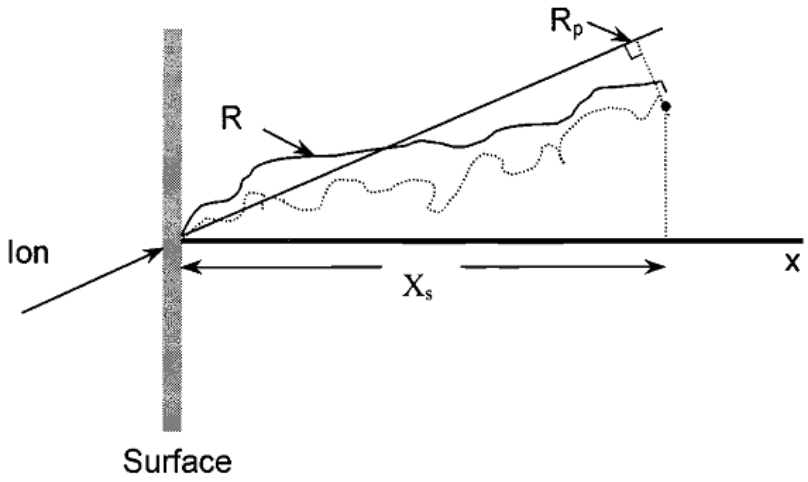

Figure 3. 2-D representation to describe the difference between ion range (R), penetration depth (X_s) and projected range (R_p). Notice that for 0^0 incident angle R_p is equal to X_s.

2.1.3 Velocity Effect

One can see in Figure 1 that similar values of electronic energy loss can be obtained with two different values of energies. The lower energy corresponds to lower velocity of ion, and the higher energy corresponds to higher velocity of ion. It was found that damage cross section caused by the same value of electronic energy loss $\left(\frac{dE}{dx}\right)_e$ is larger for lower velocity ions than that was caused by higher velocity ions which is known as velocity effect [21, 27, 28]. There are two reasons to explain this effect: First, higher velocity means higher energy which leads to the longer range of ions. Therefore, the energy is deposited in larger volume, or in other word, the energy deposition is less localized. Second, higher velocity means that at any points along trajectory, the ion has less interaction time.

2.1.4 Charge State

Slow highly charged ions (HCI) have high potential energy due to the ionization of many or even all electrons from a neutral atom. The potential energy of HCI is calculated through the total of all binding energies of the missing electrons and can reach values of several

tens up to hundreds of keV [29]. Hence, the charge state, which indicates the number of ionized electrons, determines the value of potential energy of the ions.

Upon approaching the surface, a highly charged ion is neutralized within a few to tens of femtoseconds only. The ions will resonantly capture electrons from the surface at a certain distance above the surface, which depending on the charge state of the ion, can be up to many tens of atomic units. These electrons are not captured into the inner shells but in the outer shells, thereby creating the so called hollow atoms [11, 30]. Relaxation of this hollow atom then takes place by means of Auger processes.

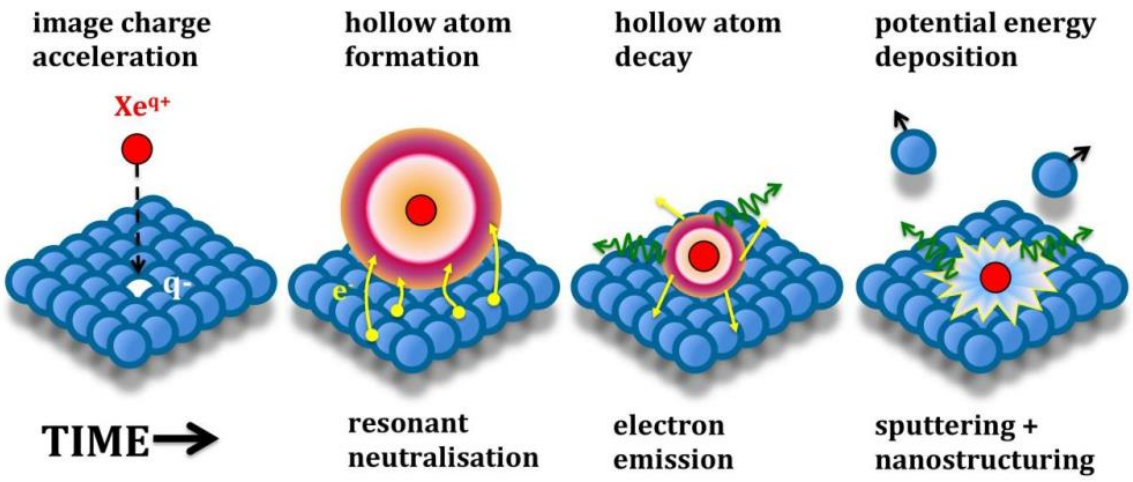

Figure 4. The visual illustration of the interaction of slow highly charged ions with solids.

Under ion irradiation, these surface phenomena are usually dominated by kinetic energy effects (kinetic electron emission, kinetic sputtering). However, the kinetic energy of HCI is relatively small (usually below 2.19×10^6 m/s) which prevents the ion penetration into the bulk [31]. The entire potential energy is then deposited into a nanometer size volume close to the surface.

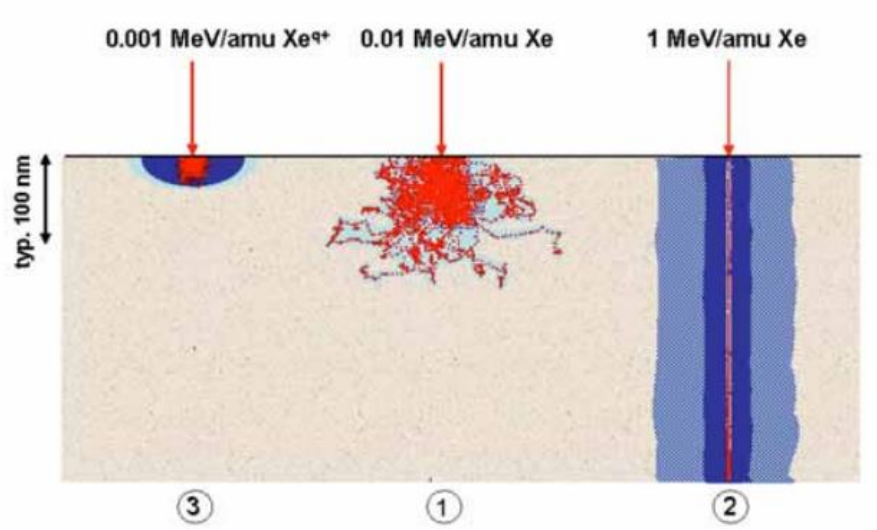

Figure 5. Comparison of material modification induced by: 1. Slow single charged ions or neutral atoms, 2. Swift ions or neutral atoms, 3. Slow highly charged ions [9].

Figure 5 depicts the damage induced by SHI, HCI and slow singly charged ions. It can be seen that with small kinetic energy, HCI creates damage localized to near-surface area due to its large potential energy. On the other hand, SHI with high electronic energy loss creates ion track deep into the bulk.

2.2 Energy Deposition and Defects Formation

The deposition of the kinetic energy of swift heavy ion lead to material modification within a cylindrical zone along the ion trajectory called ion track or latent track. The creation of these defects occurs at time scale between 10^{-13} to 10^{-3} s. In particular, diameter of the ion track is up to 10 nm, which is surrounded by radial zone up to about 0.5 μm, so called 'penumbra'. The size mainly depends on the electronic energy loss and the properties of material such as radiation sensitivity, homogeneity, atomic mobility, and electrical resistance [1]. Several models have been used to explain the formation of ion track:

1. Thermal Spike Model

Thermal spike model has been commonly used to estimate the radiation damage and to describe the track formation in insulators and some metals [32]. In this model, it is assumed that the energy is deposited instantaneously in a very small region, producing a localized increase of temperature, which spreads and cools according to the laws of classical heat conduction. Track formation due to local melting of a small region around the ion trajectory is expected if the electronic energy loss, is higher than a certain threshold value [33, 34].

Mathematical representation of this model is derived from thermal diffusion principle in the form of two non-linear differential equations in cylindrical geometry as shown below

$$\rho C_e \frac{\partial T_e}{\partial t} = \frac{\partial}{\partial r}\left(K_e \frac{\partial T_e}{\partial r} \right) + \frac{K_e}{r}\frac{\partial T_e}{\partial r} - g\left(T_e - T\right) + A(r) \tag{5}$$

$$\rho C \frac{\partial T}{\partial t} = \frac{\partial}{\partial r}\left(K \frac{\partial T}{\partial r} \right) + \frac{K}{r}\frac{\partial T}{\partial r} - g\left(T_e - T\right) \tag{6}$$

where C_e, C, K_e and K are the specific heats and thermal conductivities for the electronic and atomic systems respectively, ρ is the density of the material, r is the radius of cylindrical geometry with heavy ion path as the axis, g is the electron-phonon coupling constant, and T_e and T are the temperatures for the electronic and atomic systems, respectively. $A(r)$ is the energy deposited to electronic system at radius r [1]. The electron-phonon coupling factor g depends on the velocity of sound s in the material, thermal conductivity K and the temperature T of atomic system according to following relation

$$g = \frac{\pi^4 \left(K_b n_e s\right)^2}{18 K_e T} \tag{7}$$

where K_b is the Boltzmann constant and n_e is the electronic number density.

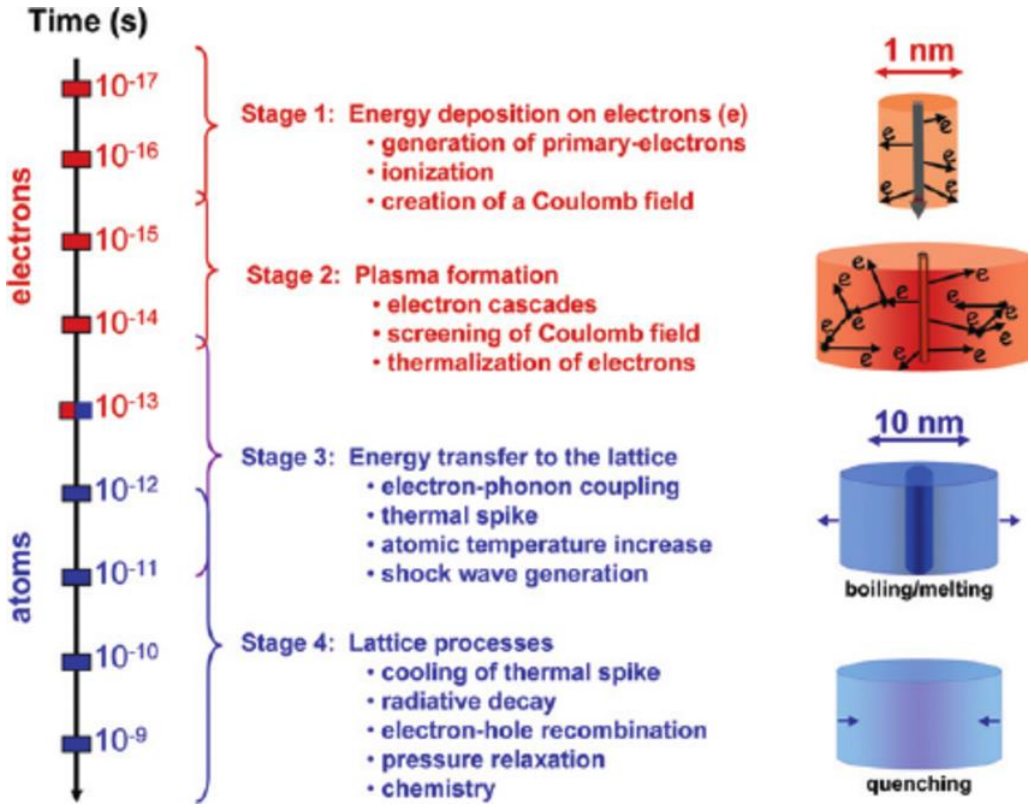

Figure 6. Schematic illustration of the time evolution of track formation for the series of processes occurring on the nanoscale during the formation of a track due to the passage of a relativistic ion through matter [35].

Thermal spike is currently the only model being able to provide at least approximate predictions on ion track formation in numerous materials. For example, numerical calculations in the framework of thermal spike model using *HEAT* code performed by Kamarou et al [36]. The overview of track radii calculated using *HEAT* code versus the corresponding experimental results for Ge, InP, and Si after irradiation at room temperature with various ions are presented in Figure 7. One can see that the thermal spike calculation and experimental results are in good agreement.

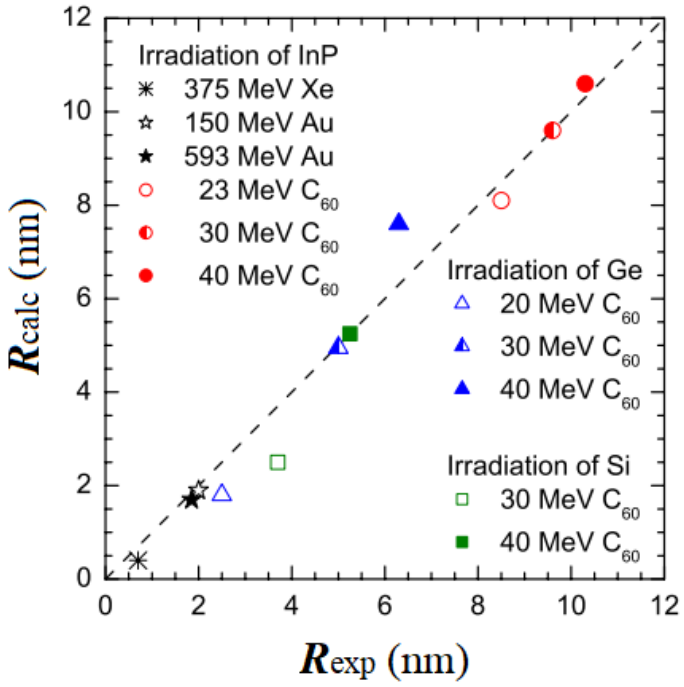

Figure 7. Track radii calculated using *HEAT* code versus experimental results for RT irradiation of InP, Ge, and Si with various ion species [36] **and cluster ion** [37].

However, since the damage formation occurs in a very short time scale, the conventional experimental methods are unable to collect a spectrum or acquiring an image even if they are applied *in situ* [38]. Therefore, there is still no experimental result available in literature directly to prove that a swift heavy ion passing through matter causes a local melting of the target material in the vicinity of the ion path [36].

2. Coulomb Explosion Model

As a result of the primary ionization along the ion beam trajectory, an ion cloud along the projectile trajectory is formed. The corresponding electrons are emitted to large distances from the ion trajectory. In metals the ion cloud is neutralized immediately ($<10^{14}$ s) after the passage of the projectile ion [39]. However, in insulators the return of the electrons to the ion cloud is inhibited if not prohibited due to electron traps. The

ion cloud, containing a large amount of stored electrostatic energy, expands explosively and becomes the driving force for an atomic collision-cascade. A high charge density in the vicinity of the ion beam trajectory sufficient to initiate a collective expansion mechanism [40].

Based on this model, two conditions should be fulfilled to obtain ion track: (1). neutralization time is longer than 10^{-14} s; and (2). local force for per unit area is larger than the mechanical tensile strength of the material [41].

$$\frac{n^2 e^2}{\varepsilon a_0^4} > \frac{E}{10} \tag{8}$$

where n is the conduction electron density, e is electron charge, a_0 is atomic spacing, ε is dielectric constant, and E is Young's modulus of the material.

It is clear from the above equation that track formation is easily possible in materials of low mechanical strength, low dielectric constant, and small inter-atomic spacing. This is the reason why coulomb explosion model could not predict the experimentally observed ion track in metals, for which the thermal spike model was invoked [1].

3. Self-Trapped Exciton Model

An exciton is a bound state of an electron-hole which is attracted to each other by the electrostatic coulomb force. In crystals, an exciton may be immobilized by its own lattice distortion field (self-trapped). When a material in which the excitons are self-trapped irradiated by energetic heavy ion, some energy transferred to the electron-hole pairs along the ion trajectory in the material leads to defect formation of the crystals.

This model suggested that the main cause of track formation is dielectric breakdown due to the induced electric field from the electrons ejected from the ion path and positive ions left after ionization [42]. Track formation occurs when the incident ion exceed some stopping power threshold.

2.3 Ion-Induced Damage in Semiconductor

Track formation due to SHI irradiation in insulating materials as well as in some metals can be adequately described by thermal spike model. However, the behavior of semiconductors under SHI irradiation seems to be different from that of metals or insulators [34]. The major consequences of ion induced excitations are enhanced processes like diffusion, or the production of metastable, non-equilibrium states of defects [42]. In addition, modification of the physical properties of the irradiated material.

Under SHI irradiation a strong competition between damage evolution, transformation and annealing occurs in the semiconductors. Which of these processes dominates and whether tracks are formed or not depends on a variety of material parameters [21]. Therefore, SHI irradiation in semiconductors also highly depends on the irradiation temperature.

Many experiments reported that insulators are in general more sensitive to SHI-induced damage than semiconductors, which in turn are more sensitive than conductors and superconductors [32, 43]. As in insulators and metals, the formation of visible tracks in semiconductors requires certain (material dependent) threshold of the electronic energy deposition to be surpassed. These threshold values are usually larger than the ones observed in various insulators.

Ion tracks were observed in InP, InAs, InSb and GaSb after irradiation with swift Xe, Au and Pb ions with electronic energy loss above ~19 keV/nm. Whereas the tracks in InSb are almost recrystallized, they are amorphous in InP and GaSb. For InP an electronic energy loss threshold of ~13 keV/nm was observed. Furthermore, at electronic energy loss around 20 keV/nm the track evolution depends on the ion fluence, i.e. not each impinging ion produces a visible track and even predamage was necessary to form tracks [21].

In contrast to the above semiconductors, amorphous tracks were not observed in Si, Ge and GaAs by irradiation with monoatomic ion beams but it is easily formed in case of MeV cluster ions having higher electronic energy loss [20, 37, 44]. In this case, the electronic energy loss reaches very high value (about 50 keV/nm), as well exhibiting highly deposited energy density, which cannot be obtained in case of monoatomic SHI. As possible reasons for the low radiation sensitivity of some semiconductors it may be suspected that either SHI does not produce significant damage upon impact or damage is created and then annealed immediately after or during subsequent irradiation.

In order to understand the mechanism responsible for the SHI-induced damage in semiconductors, the extended thermal spike model was used by many researchers. This model takes into account the radial distribution of the dose and also gives a more detailed description of the energy transfer processes from the ion to the electronic system of the target atoms. It described successfully the track formation and the damage accumulation in the III-V binary semiconductor InP [6].

Overall, the results available for swift heavy ion irradiation in semiconductors do not show clear correlation between the formation of ion track in various semiconductors and their

macroscopic material parameters such as melting temperature, thermal conductivity, or band gap energy. Qualitatively, most of the experimental data regarding damage creation can be understood in the framework of the thermal spike approach [21].

CHAPTER 3

EXPERIMENTAL METHODS

3.1 Gallium Phosphide (GaP)

In this study, we use several samples of 10 mm × 10 mm and 0.5 mm thick single crystals (111) of undoped gallium phosphide (GaP) from MTI Corporation. GaP is a type III-V wide-bandgap semiconductor (2.26 eV) that currently attracts high interest due to its application as semiconductor laser and light emitting diode (LED) [45]. Due to its high second order nonlinear coefficient, high thermal conductivity and broad transparency range, GaP is considered as an excellent material for nonlinear optical applications. Moreover, it has a high refractive index, which enhances the rapid variation of electric field across GaP air interfaces, contributing to the strong surface optical nonlinearity [46, 47].

GaP has zinc blende crystal structure with lattice constant 5.45 Å. Pure single crystal wafers of GaP are clear orange while strongly doped ones appear darker. It does not dissolve in water and is odorless.

Table 1. Chemical and mechanical properties of gallium phosphide

Chemical Formula	**GaP**
Molecular Weight	100.7 g/mole
Band Gap Energy	2.26 eV (indirect)
Carrier Concentration	$\mathbf{4{\sim}6 \times 10^{16}}$ /cm^3
Crystal Structure	Cubic : Zinc Blende
Lattice Constant	5.45 Å
Melting Point	1480 ^{0}C
Density	4.13 g/cm3
Young's Modulus	$\mathbf{8.8 \times 10^{11}}$
Thermal Conductivity	1.1 W cm^{-1} ^{0}C^{-1}
Refractive Index (589 nm @293 K)	3.02

3.2 Ion-Irradiation

3.2.1 Ion Beam Facilities

i. Swift Heavy Ions

The ion irradiation was performed at two research facilities:

- **Universal Linear Accelerator (UNILAC) at GSI Darmstadt, Germany**

At GSI accelerator facility, all ions, up to uranium, can be accelerated. From the ion source, the ions are injected to the 120 m long UNILAC which can accelerate the ions up to ~20% speed of light. The kinetic energy range of the ions accelerated by UNILAC is 2-14 MeV/u. From the UNILAC, the ions can be used either for experiments in x0 and M branch or injected to the ring accelerator SIS 18 for further ion acceleration up to 90% speed of light corresponds up to 2 GeV/u kinetic energy. The samples in this work were irradiated in x0 cave which is located at the end of UNILAC experimental hall (Figure. 8) [48].

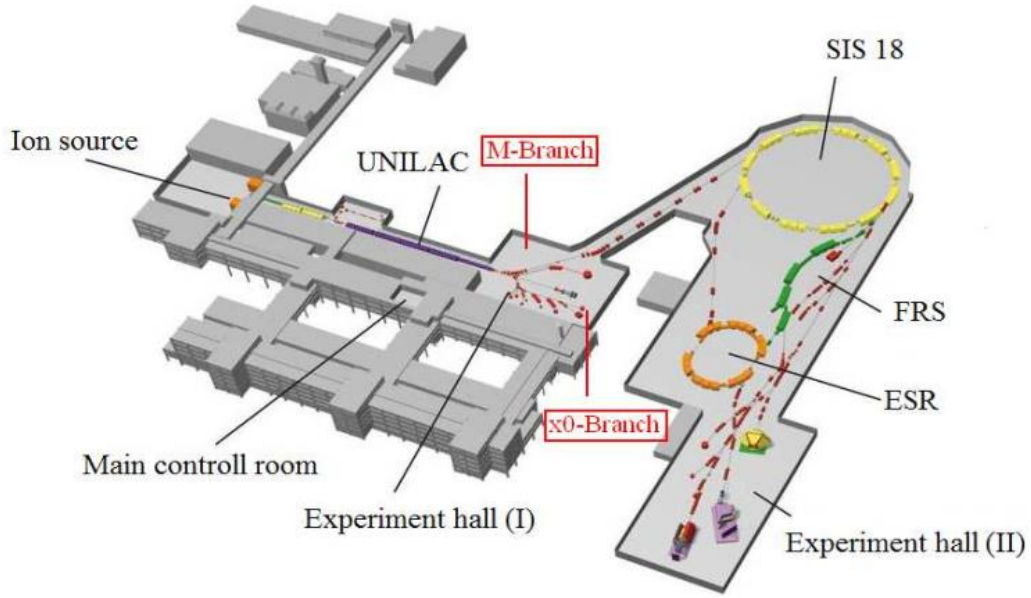

Figure 8. Schematic structure of GSI accelerator facilities for experiments using swift heavy ions.

- **6 MV Tandem Accelerator at HZDR Dresden, Germany**

This accelerator operates via a Cockcroft-Walton type high voltage generator providing the terminal voltage up to 6 MV. The energy range of the ions accelerated by this accelerator is about 0.6-54 MeV which depends on the charge state of the ions [49].

Figure 9. 6 MV tandem accelerator.

ii. Slow Highly Charged Ions

The samples were irradiated at the Electron Beam Ion Trap (EBIT) facility of HZDR, Dresden. Dresden EBIT uses a strong magnetic field along with high energy electron beam which induce a space charge to spatially confine ions in a small region (trapped). The powerful electron beam with currents up to 50 mA are focused to a small diameter of 200 μm and targeted to these trapped ions. By continuous bombardment by the electron beam, the ions lose their outer electrons

(ionize). Ionizations occur as long as the binding energy of a given bound electron is below the kinetic energy of the electron beam (e.g. up to 15 keV) [50].

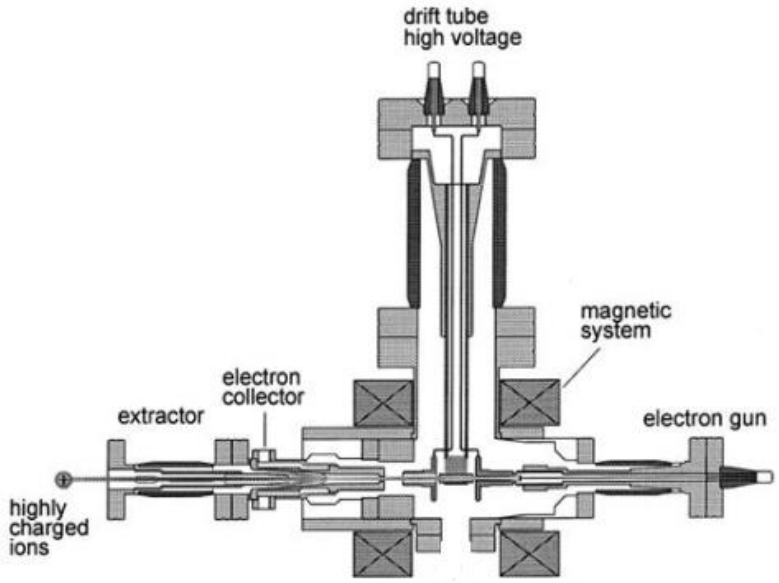

Figure 10. Schematic diagram of the main components of Dresden EBIT [51].

3.2.2 Irradiation Parameters

To study the slow highly charged ions (HCI) and swift heavy ions (SHI) induced modifications, the samples were irradiated with ions of different charge states, kinetic energies, and fluences. For HCI, the samples were irradiated with 114 keV Xe^{q+} ions (q=33-40) of ion fluence $\phi = 1 \times 10^9$ cm-2. For SHI, part of the used samples was irradiated with I ions of kinetic energies between 1 MeV and 54 MeV from the tandem accelerator of HZDR, Dresden. The irradiation of the other part of the samples was performed using Au ions from UNILAC, Darmstadt. In addition to the used Au primary kinetic energy of 1.16 GeV, 240 MeV ions were utilized by using Al degrader above the

irradiated samples. The ion fluence for SHI irradiations are varied between 1×10^{10} and 1×10^{14}. In all cases, the irradiations were performed at room temperature.

To estimate the nuclear and electronic energy loss as well as the projected ion range, we used SRIM-2013 software without considering the secondary energy loss to the target electrons. The results are summarized in Table 2.

Table 2. Ion irradiation parameters obtained using SRIM code.

Ions	E_{pot} (keV)	E_{kin}	$\left(\frac{dE}{dx}\right)_e$ (keV/nm)	$\left(\frac{dE}{dx}\right)_n$ (keV/nm)	R_p (μm)
virgin	-	-	-	-	-
Xe^{33+}	**21.2**	**114 keV**	**0.3**	**2.75**	**0.01**
Xe^{36+}	**27.8**	**114 keV**	**0.3**	**2.75**	**0.01**
Xe^{38+}	**33.0**	**114 keV**	**0.3**	**2.75**	**0.01**
Xe^{40+}	**38.5**	**114 keV**	**0.3**	**2.75**	**0.01**
I^{+}	-	**1 MeV**	**1**	**2.1**	**0.28**
I^{3+}	-	**6 MeV**	**1.95**	**0.94**	**1.87**
I^{9+}	-	**54 MeV**	**10.3**	**0.2**	**9.6**
Au^{25+}	-	**240 MeV**	**18.3**	**0.14**	**25.1**
Au^{25+}	-	**1.1 GeV**	**29.5**	**0.05**	**50.7**

3.3 Analyzing Techniques

3.3.1 Atomic Force Microscopy (AFM)

i. Operation Principles

Atomic force microscope (AFM) is a sophisticated tool to obtain high-resolution surface topographical images of a material. It is also capable to determine the mechanical properties and composition of the materials. AFM covers a wide range of applications, from materials science to biology. AFM can be operated in a number of environments including ambient air, ultra high vacuum (UHV), and liquids.

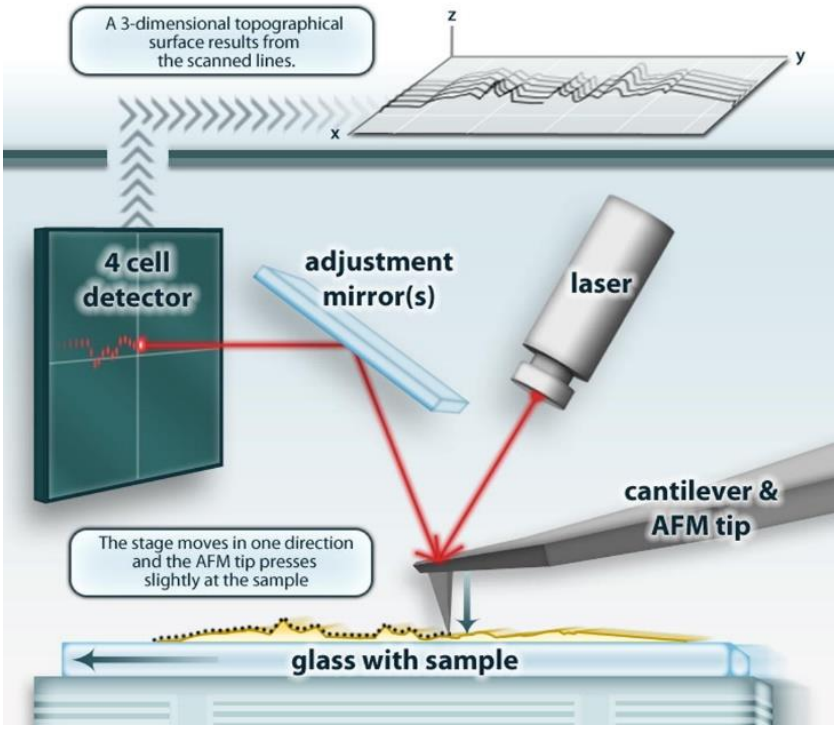

Figure 11. Schematic diagram of for AFM measurement.

The main parts of the AFM are a sharp tip, a microcantilever, a laser, and a photodetector (Figure.11). Most commonly, the sharp tip is attached to a flexible microcantilever which bends under the influence of force. The bending of microcantilever leads to a change in

angle of inclination, measured by reflecting a laser beam off of the microcantilever towards a position-sensitive detector, the output of which displays any movements of the laser spot [52, 53].

There are several modes to perform surface analysis using AFM, each with its own merits and shortcomings:

1. **Contact Mode**

   In contact mode the surface topography is scanned, where the tip is always in contact with the surface. Height information can be obtained by directly measuring the cantilever deflection. However, to avoid the nonlinear relation of deflection and surface height, a control loop can be used to keep the deflection constant by adjusting the scanner position perpendicular to the sample surface. The major shortcoming of contact mode is the possibility of abrasions and damage of soft samples due to the friction which occurs between the tip and sample surface. However, it gives an additional measurable quantity, the lateral force, which leads to microcantilever torsion deflecting the laser beam perpendicular to the axis of bending. Thus, lateral force microscopy maps the friction between the tip and sample.

2. **Noncontact Mode**

   In noncontact mode the cantilever is prompted as a driven oscillator slightly above the resonance frequency. Attractive dispersion forces (van der Waals) effectively lower the reset force of the oscillator as a function of the sample-tip distance, reducing its resonance frequency. A control loop is employed to keep the oscillation amplitude constant by adapting the actuation frequency. In comparison to contact mode, the

resolution in this mode is reduced due to the long range of the participating forces. However, it is the most sparing AFM mode which is suitable for soft biological samples.

3. Tapping Mode

In tapping mode, or intermediate mode, the microcantilever is oscillated at or near its mechanical resonant frequency near the surface. The amplitude of this oscillation is used as a feedback signal. If the microcantilever passes a hillock, for example, the oscillation amplitude will momentarily decrease, causing the z-piezo to move the tip against the surface to restore the preset amplitude. In tapping mode the phase shift between the actuation signal and the cantilever oscillation can also be measured, yielding a dampening factor depending on sample elasticity. Chemical functionalization of the tip allows to map specific chemical properties of the sample surface, through phase-shifts caused by local stickiness of the surface.

ii. Experimental

The irradiated samples were investigated by atomic force microscopy (AFM). The microscope was operated using tapping mode in air utilizing Nanosensors PPP-NCLR probes of tip radius less than 10 nm. The Nanotec Electronica SL WSxM software [54] (version 4.0 beta 9.0) and Gwyddion software [55] were utilized for image processing and dimension analysis of the AFM topographic images.

3.3.2 Rutherford Backscattering Spectrometry (RBS)

i. Operation Principles

RBS is the most commonly used ion beam analysis technique. The samples are bombarded with ions at kinetic energy typically in the range of 0.5-4 MeV. Usually protons, ^{4}He, and sometimes Li ions are used as projectiles at backscattering angles of typically 150^{0}-170^{0}. Different angles or different projectiles are used in special cases [56, 57].

The mechanism relies on the fact that the energy of an elastically backscattered particle depends on the mass of the target atom (kinematic factor) and on the depth at which the scattering took place (energy loss on the way to and from the point of interaction). The use of energy sensitive detector allows us to determine the elemental composition of the sample near the surface, as well as enabling depth profiling of individual elements.

RBS is quantitative method which does not require reference sample. It has a good depth resolution of the order of several nm, and a very good sensitivity for heavy elements of the order of parts-per-million (ppm). The analyzed depth is typically about 2 μm for incident He ions and about 20 μm for incident protons. The drawback of RBS is the low sensitivity for light elements, which often requires the combination with other nuclear based methods like nuclear reaction analysis (NRA) or elastic recoil detection analysis (ERDA).

The identification of a certain atomic mass in the sample is based on the kinematic factor K

$$K = \frac{E_1}{E_0} = \left[\frac{\left(m_2^2 - m_1^2 \sin\theta\right)^{1/2} + m_1 \cos\theta}{\left(m_1 + m_2\right)} \right] \tag{9}$$

where E_0 is the energy of incident ion of mass m_1, E_1 is the energy of backscattered ion, m_2 is the mass of target atom and θ is the scattering angle.

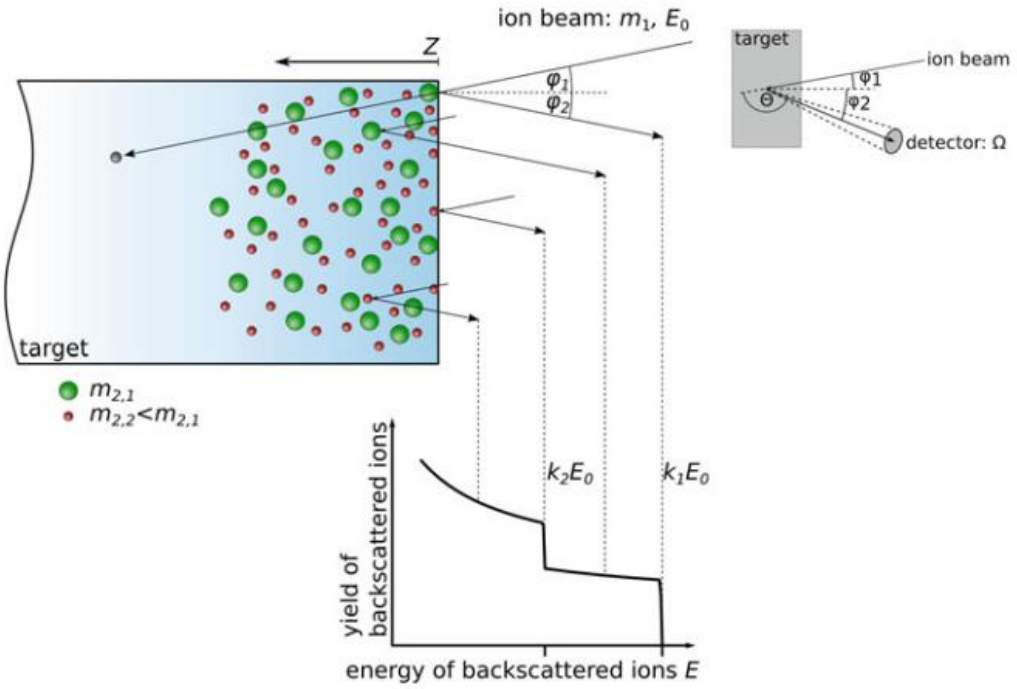

Figure 12. Schematic representation of the geometry of RBS experiments and origin of RBS spectrum for material composed of two atomic species with masses $m_{2,2} < m_{2,1}$.

In the case of mass discrimination, the signal from an atom at the sample surface will appear in the energy spectrum at a position $E_1 = KE_0$. In case of depth profiling, the signal from atoms of the same mass below the sample surface will be shifted by the amount of energy lost while the projectiles pass through the sample.

The yield of backscattered ions increases significantly with increasing atomic number of the target atoms and with decreasing ion energy. The yield of ions backscattered from the different atoms of the target adds up and finally forms the RBS random spectrum.

When the ions enter a monocrystalline solid in direction of a low-index axis, the yield of backscattered ions adds up and forms the aligned spectrum. Along the axis, the atoms of the crystal are arranged in rows which form channels. Within these channels the ions perform a guided movement due to the periodic atomic potentials which is called channelling effect. The consequence of channelling is reduction of the probability for the occurrence of backscattering events and thus, the significant decrease of the yield of backscattered ions.

Channeling of ions can be used to analyze a crystalline sample for lattice damage. If atoms within the target are displaced from their crystalline lattice site, this will result in a higher backscattering yield in relation to a perfect crystal. By comparing the RBS spectrum from the sample obtained in aligned orientation (represent perfect crystal) with the one obtained in random orientation (represent amorphous sample), it is possible to determine the extent of crystalline damage in terms of a fraction of displaced atoms [58].

ii. Experimental

A 1.7 MeV $^{4}He^{+}$ ion beam from the 2 MV van de Graaff accelerator at the HZDR, Dresden was used in the performed experiments. The samples were mounted on a high precision 5-axis goniometer located in a vacuum chamber. The backscattered $^{4}He^{+}$ ions were detected by means of a Si barrier detector at 170^{0} backscattering angle. The facility was used for RBS and RBS/c measurements, where c denotes dechanneling.

3.3.3 X-ray Photoelectron Spectroscopy (XPS)

i. Operation Principles

XPS (X-ray Photoelectron Spectroscopy) has been widely used for analyzing the near-surface chemistry of a material. XPS allows us to determine the elemental composition, empirical formula, and oxidation state of the elements within a material. The basic idea of XPS is measuring the kinetic energy of the electrons ejected from a surface of the sample during bombardment by X-ray (Figure.13). Since electrons of each element have their own specific binding energies, we can calculate the binding energy of the photoelectrons and identify the elemental composition of the sample by applying energy conservation.

$$BE = hf - KE - \phi \tag{10}$$

where BE is the binding energy, hf is the energy of the photon, KE is the kinetic energy of photoelectron, and ϕ is the work function which depends on the spectrometer (typically 4-5 eV).

The exact binding energy of an electron depends not only upon the level from which photoemission is occurring, but also depends on the oxidation state of the atom and the local chemical environment. Atoms of a higher positive oxidation state exhibit a higher binding energy due to the extra coulombic interaction between the photo-emitted electron and the ion core. This ability to discriminate between different oxidation states and chemical environments is one of the major strengths of the XPS technique.

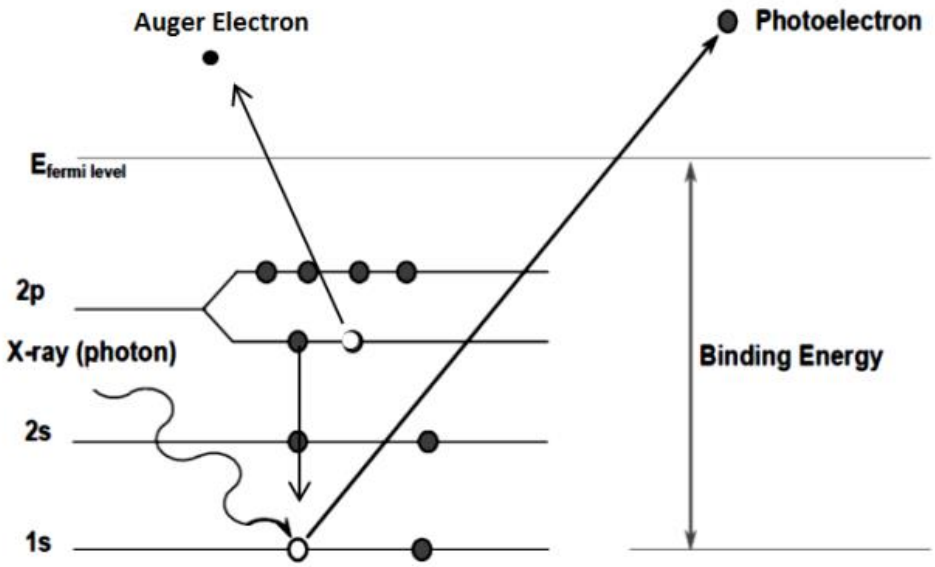

Figure 13. Photoelectric effect as the basis of XPS technique to analyse the surface of materials.

For an electron of intensity I_0 emitted at a depth d below the surface, the intensity is attenuated according to the Beer-Lambert law due to inelastic collisions, recombination, excitation of the sample, and recapture or trapping in various excited states within the material. So, the intensity I_s of the same electron as it reaches the surface is given by

$$I_s = I_0 e^{-d/\lambda} \tag{11}$$

where λ is the inelastic mean free path of the electron in solid materials. The value of λ is in the range of 1-3.5 nm for Aluminium K-α bombardment. In XPS, sampling depth is defined as the depth from which 95% of all photoelectrons are scattered by the time they reach the surface, which is 3λ or about 3-10 nm [59]. Since XPS is a surface sensitive technique, it should be performed under ultra high vacuum (UHV) conditions.

ii. Experimental

Selected samples were investigated using Escalab 250 Xi X-ray photoelectron Spectrometer manufactured by Thermo Fisher Scientific. Escalab 250 Xi uses monochromatic Aluminum K-α as X-ray source with energy of 1487.6 eV and intrinsic FWHM (Full Width at Half Maximum) of 0.43 eV.

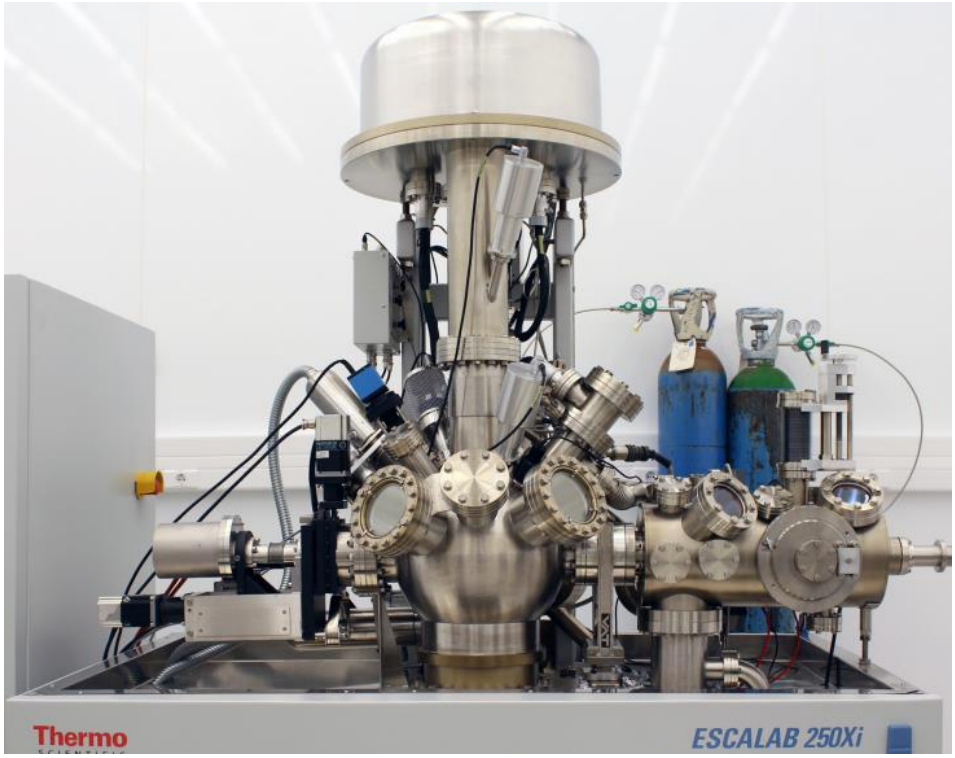

Figure 14. Photograph of Escalab 250 Xi Spectrometer manufactured by Thermo Fischer Scientific.

3.3.4 UV-Visible Spectroscopy

i. Operation Principles

UV-vis spectroscopy has been used for a long time to study optical properties of materials. The mechanism of UV-vis spectroscopy is pretty straightforward. A beam of light from a visible and UV light source is separated into its component wavelengths by a prism or diffraction grating. Each monochromatic beam is split into two equal intensity beams by a half-mirrored device. One beam, the sample beam, passes through a small transparent container containing the irradiated sample. The other beam, passes through an identical container containing the reference sample (blank). The intensity of light beams are then measured by electronic detectors. The intensity of the beam transmitted by the reference is defined as T_0 and the intensity of the beam transmitted by the sample under study T is defined as

$$T = T_0 \exp\left(-\alpha d\right) \tag{12}$$

where α is the absorption coefficient and d is the thickness of the sample.

Since the reference container is left blank, the transmission of the reference is maximum $T_0 = 1$. The optical absorption coefficient is then given by [14]

$$\alpha = \frac{1}{d} \ln\left(\frac{1}{T}\right) \tag{13}$$

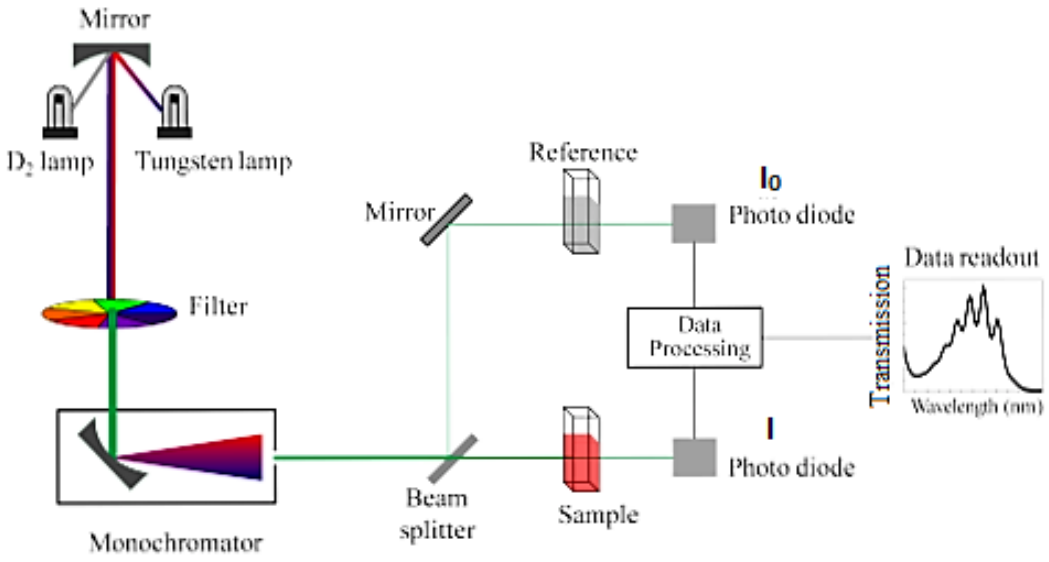

Figure 15. The schematic mechanism of UV-vis spectroscopy.

ii. Experimental

The virgin and all irradiated samples were inspected with UV-vis spectrometer at room temperature in the wavelength region of 190-2500 nm. The spectrometer was operated in the transmission mode, where the spectrum is represented as graph of the transmission as function of wavelength.

CHAPTER 4

RESULTS AND DISCUSSIONS

4.1 Atomic Force Microscopy (AFM)

4.1.1 Slow Highly Charged Ions

Surface features in the measured AFM topographic images of the virgin GaP sample (Figure. 16) are only grooves caused by polishing. Surface roughness of the virgin sample was estimated to be ~0.2 nm which should be considered as the minimum detection limit for hillocks height measurement.

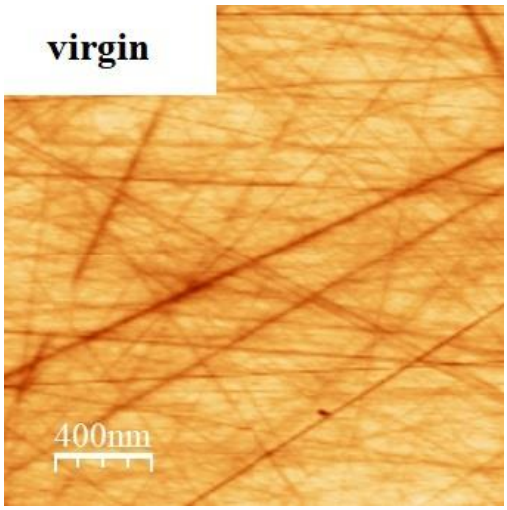

Figure 16. AFM topographic image $2 \times 2\ \mu m^2$ of single crystal GaP virgin sample.

The topographic AFM images for GaP samples irradiated with 114 keV highly charged Xe^{q+} ions of various charge states (q=33, 36, 38, and 40) show no noticeable topographic changes (Figure. 17) in comparison to the virgin. These results showed that highly charged

xenon ions carrying the highest available charge state (q =40 correspond to potential energy of 38.5 keV), were not able to create an observable surface nanostructures in GaP. For surface nanostructuring with HCI, the potential energy plays similar role as electronic energy loss for SHI. Therefore, it was concluded that the potential energy threshold for creation of surface nanostructure is above 38.5 keV. This value is in agreement with the one observed for the similar material e.g. GaN [4].

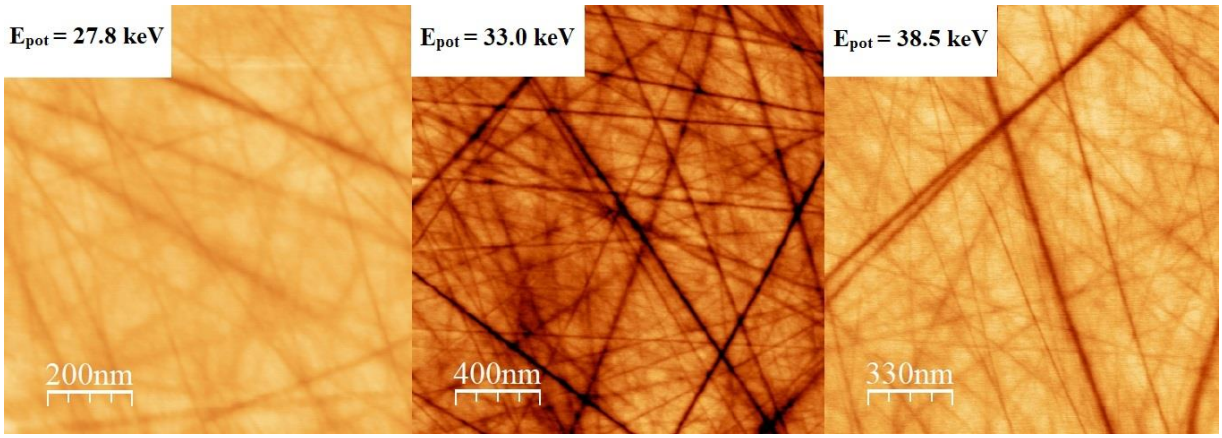

Figure 17. AFM topographic images of GaP single crystals irradiated with 10^9 ions cm^{-2} slow highly charged Xe of various charge state. Potential energy is shown in each case.

4.1.2 Swift Heavy Ions

The topographic images of all GaP samples irradiated with SHI at the UNILAC (Au ions of kinetic energies 240 MeV and 1.16 GeV corresponding to $\left({}^{dE}/_{dx}\right)_e$ of 18.3 and 29.5 keV/nm, respectively) showed nanohillocks protruding from the surface. The hillocks are shown in the images as the bright spots. For sample irradiated with 240 MeV Au ions (Figure. 18), the average width and height of the hillocks are around 26 nm and 0.8 nm, respectively. In the case of GaP irradiated with 1.16 GeV Au ions (Figure. 19), the average width and height of the hillocks are around 28 nm and 0.5 nm, respectively.

The width of a hillock was determined by defining two opposite points representing the regions where a height profile line (Left and Right foot) through the hillock maximum merge with the undamaged surface plane.

Approximating the hillocks as segment of a sphere (spherical cap), the volume of the hillocks can also be approximated using the following formula

$$V = \left(\frac{\pi}{6}H\right)\left(\frac{3}{4}D^2 + H^2\right) \tag{14}$$

where D and H stand for diameter and height of the hillocks, respectively. The average volume of hillocks in GaP surface after irradiation with 240 MeV and 1.16 GeV gold ions are around 212 $nm^3$and 185 nm^3, respectively.

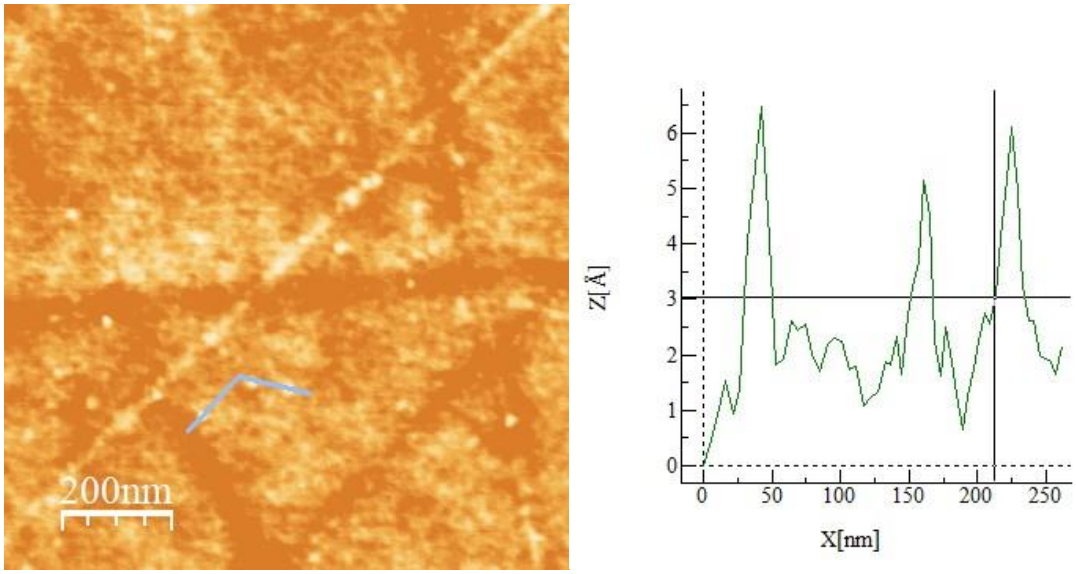

Figure 18. Topographic images ($1\ \mu m \times 1\ \mu m$) of GaP sample irradiated with 240 MeV Au ions corresponding to $\left(dE/dx\right)_e$ of 18.3 keV/nm (left) and the line profile of the selected region (right).

In contrast to swift gold ions, AFM topographic measurements did not show any topographic features on GaP surface after irradiation at the 6-MV tandem accelerator with

kinetic energy below 54 MeV iodine corresponding to $\left(dE/dx\right)_e$ of 10.3 keV/nm. Therefore, the $\left(dE/dx\right)_e$ threshold for hillock creation in GaP then should be between 10.3 keV/nm and 18.3 keV/nm. However, this is in contradiction to previous result where the presence of hillocks in the surface of GaP can be measured by AFM even with smaller $\left(dE/dx\right)_e$ of 9.3 keV/nm [60]. It is important to mention that the presented AFM results on the surface modification were induced by SHI with applied ion fluence of 5×10^9 and 10^{10} cm^{-2} for gold and iodine ions, respectively. The use of these values is intended to study the evolution of surface nanostructures as a function of electronic energy loss induced by single ion impact. The discrepancy with the results presented in Ref [60] can be due to the difference in the applied ion fluence. In that work, the authors were using higher ion fluence of $\phi = 10^{12}$ cm^{-2} where the effect of multiple ion impacts should be considered.

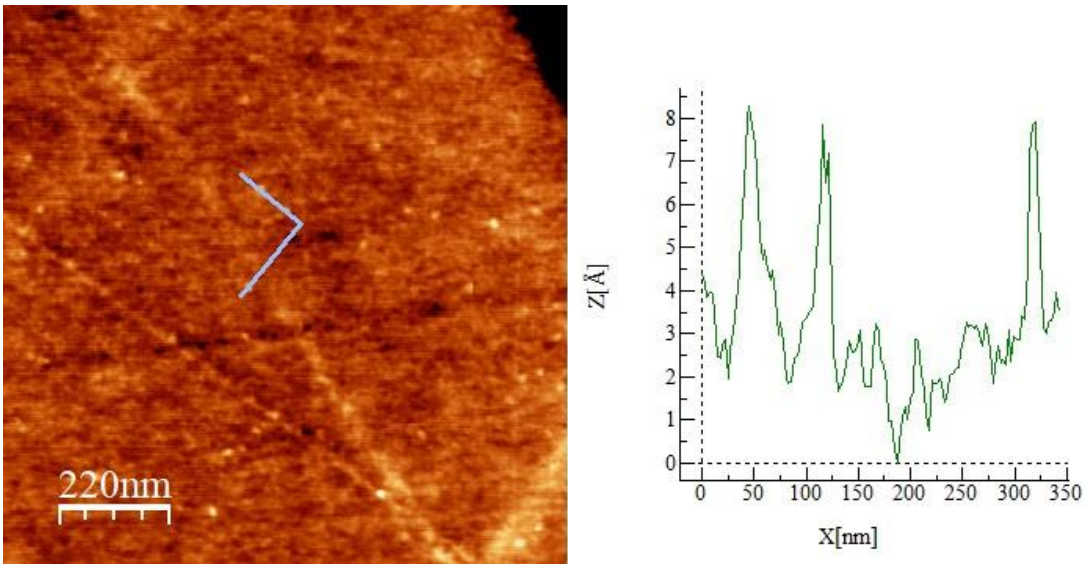

Figure 19. Topographic images ($1.1\ \mu m \times 1.1\ \mu m$) of GaP sample irradiated with 1.16 GeV Au ions corresponding to $\left(dE/dx\right)_e$ of 29.5 keV/nm (left) and the line profile of the selected region (right).

4.2 Rutherford Backscattering Spectrometry (RBS)

Figure 20 shows the aligned and random RBS spectra for GaP samples after irradiation with 1 MeV I^+ of various ion fluence Φ. The analysis of RBS spectra is usually focused only on the high-energy part of the spectra which results from the heavier component of the material. In this case, gallium is the heavier element in which its corresponding RBS spectra lies at channel 570 – 775.

The backscattered yield of the aligned spectra increases with the ion fluence. At ion fluence of $\Phi = 1 \times 10^{13}$ cm^{-2}, a sharp increase in the backscattered yield indicating the creation of a significant damage of the GaP crystalline structure. The aligned spectra reaches a random level at $\Phi = 1 \times 10^{14}$ cm^{-2} which is usually considered as an indication of the formation of amorphous layer [58, 61]. At this particular energy (1 MeV), the nuclear energy loss is dominating over the electronic energy loss and the projected ion range is $R_p = 0.28\ \mu m$. The distribution of the displaced atoms (Figure. 23a) are located within the RBS sampling depth for the incident He ions.

Usually, the nuclear energy deposition is expressed in terms of number of displacements per lattice atom n_{dpa} according to

$$n_{dpa} = \frac{\phi N^*}{N_0} \tag{15}$$

where ϕ is the ion fluence, N^* is the number of displacements per ion per unit length obtained using TRIM code, and N_0 is the atomic density of the irradiated material. The

estimation of damage accumulation is calculated in terms of the difference in the minimum yield $\Delta\chi_{min}$ following [6, 61]

$$\Delta\chi_{\min} = \frac{\sum_{n=570}^{775} Y_{aligned}^{irradiated} - \sum_{n=570}^{775} Y_{aligned}^{virgin}}{\sum_{n=570}^{775} Y_{random} - \sum_{n=570}^{775} Y_{aligned}^{virgin}} \quad (16)$$

where $Y_{aligned}^{virgin}$ and $Y_{aligned}^{irradiated}$ are the RBS yield in the aligned direction of the virgin and irradiated samples, respectively. Y_{random} is the RBS yield of the random spectra and n is the channel number. $\Delta\chi_{min} = 0$ and $\Delta\chi_{min} = 1$ correspond to undamaged and heavily damaged (completely amorphized) material, respectively.

The calculated values of n_{dpa} and $\Delta\chi_{min}$ for 1 MeV iodine irradiations are tabulated in table below. One can clearly see that the damage accumulation increases until amorphization occurs with the increasing n_{dpa} at constant kinetic energy of ion. This gives evidence that the formation of amorphous layer arises due to multiple overlap of damaged zones induced by the nuclear energy loss.

Table 3. Calculated values of n_{dpa} and $\Delta\chi_{min}$ for GaP irradiated with 1 MeV iodine.

Ion Fluence ϕ (ions cm^{-2})	1×10^{11}	1×10^{12}	1×10^{13}	1×10^{14}
n_{dpa}	0.001	0.01	0.106	1.06
$\Delta\chi_{min}$	0.021	0.056	0.607	0.96

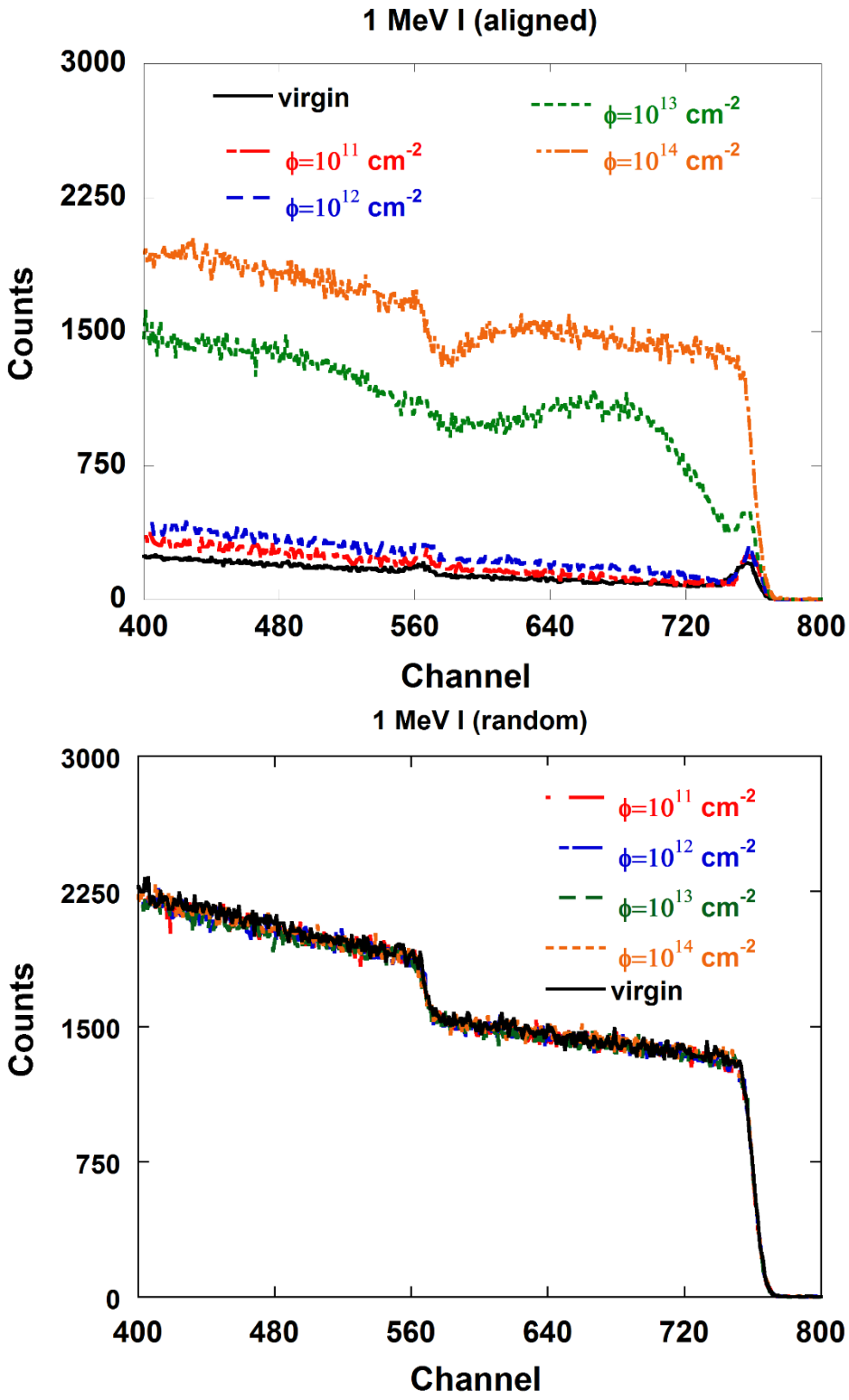

Figure 20. Aligned (top) and random (bottom) RBS spectra of GaP irradiated with various fluences of 1 MeV I^+ ions at room temperature.

In the case of RBS/c measurement of GaP irradiated with 54 MeV I (Figure. 20) and 1.16 GeV Au (Figure. 21) amorphization was not observed. Projected ion ranges for GaP irradiated with 54 MeV I and 1.16 GeV Au were calculated to be $R_p = 9.6\ \mu m$ and $R_p = 50.7\ \mu m$, respectively. One can see that the distribution of the displaced atoms for 54 MeV I (Figure. 24a) and 1.16 GeV gold irradiation (Figure. 25a) are outside the range of RBS sampling depth.

Despite the huge electronic energy deposition in the near surface region in case of 54 MeV I (Figure. 24b) and 1.16 GeV Au (Figure. 25b), the amorphized layer was not observed. It might be implied that for GaP, the amorphization can only be achieved by the nuclear energy loss via elastic collision of ion with the target atom. This is in agreement with the results presented in Refs [36] and [61].

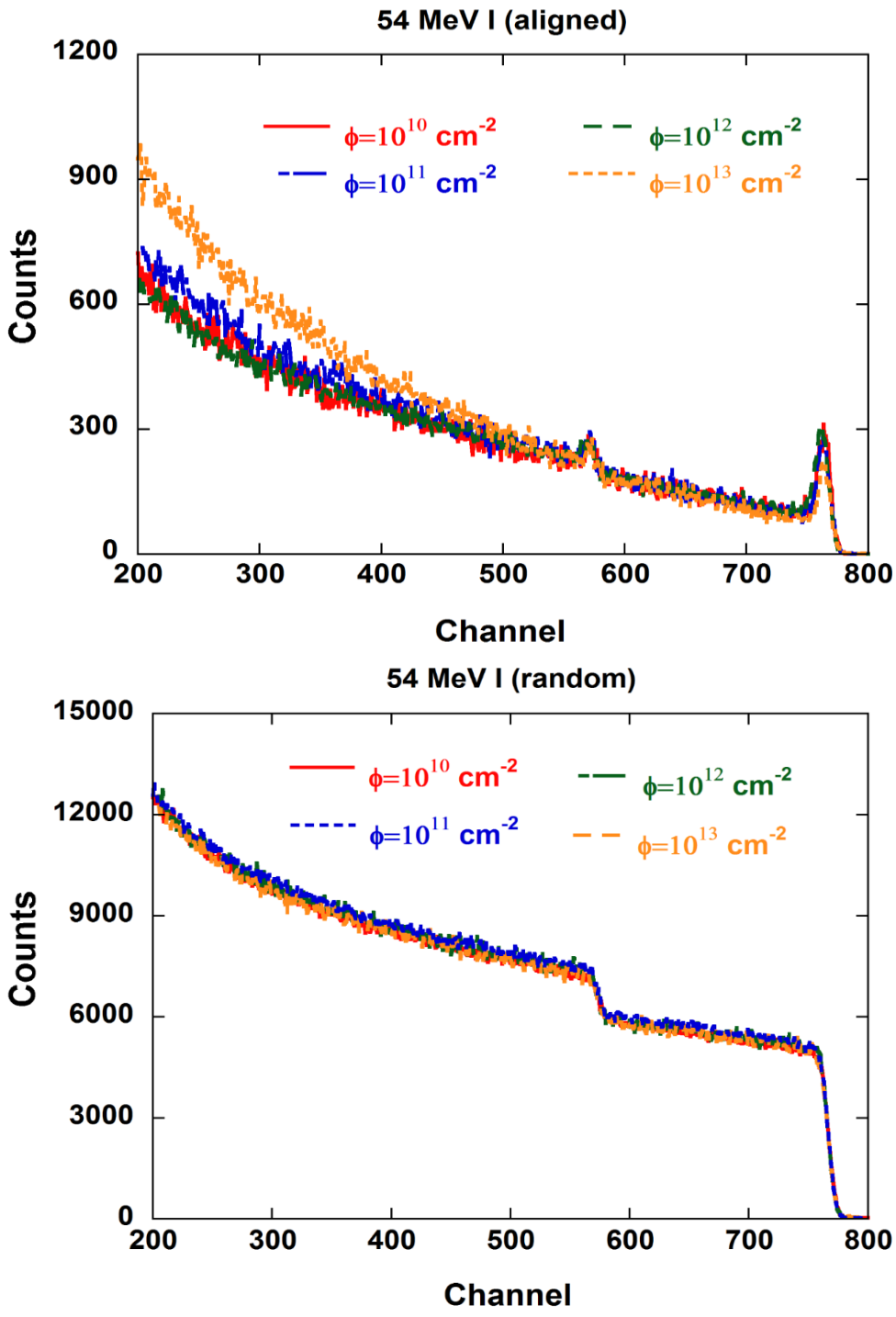

Figure 21. Aligned (top) and random (bottom) RBS spectra of GaP irradiated with various fluences of 54 MeV I^{9+} ions at room temperature.

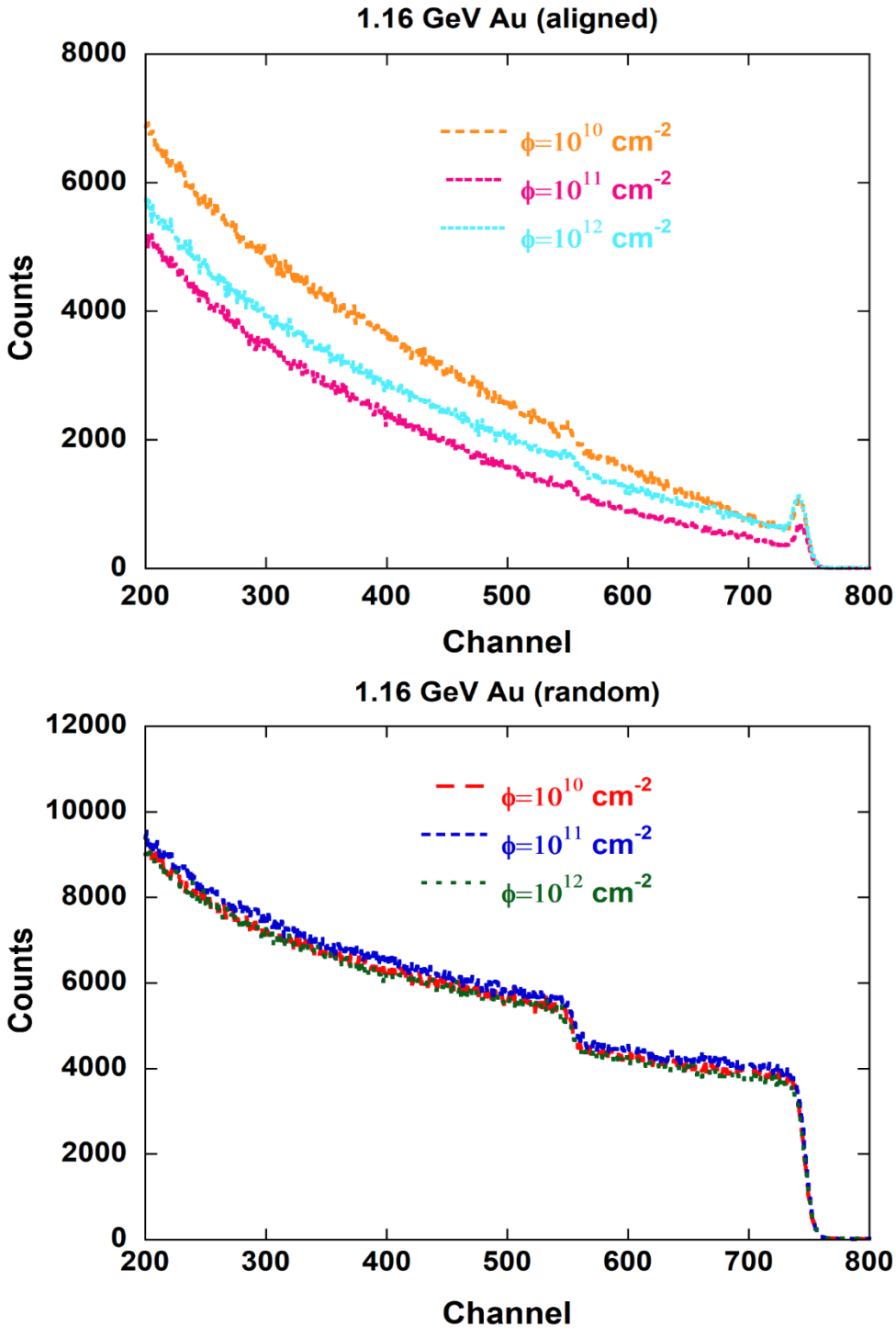

Figure 22. Aligned (top) and random (bottom) RBS spectra of GaP irradiated with various fluences of 1.16 GeV Au^{25+} ions at room temperature.

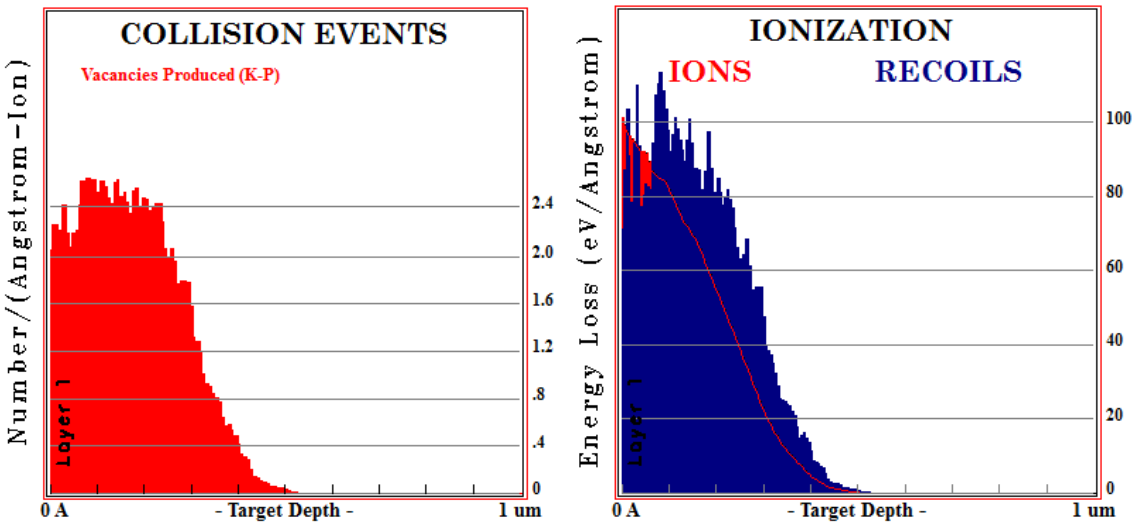

Figure 23. TRIM calculation for the distribution of vacancies (left) and energy loss (right) of GaP irradiated with 1 MeV I ions.

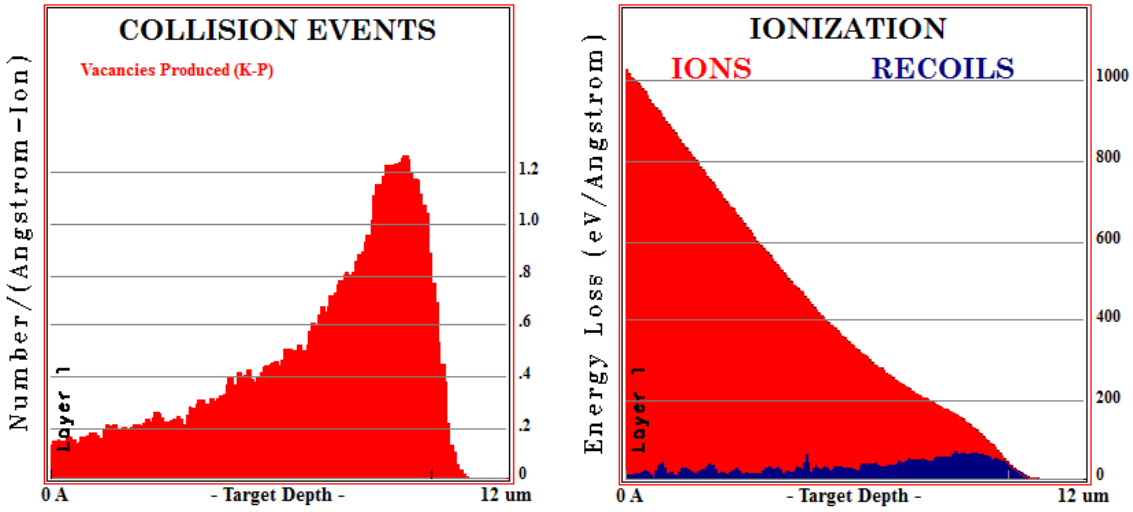

Figure 24. TRIM calculation for the distribution of vacancies (left) and energy loss (right) of GaP irradiated with 54 MeV I ions.

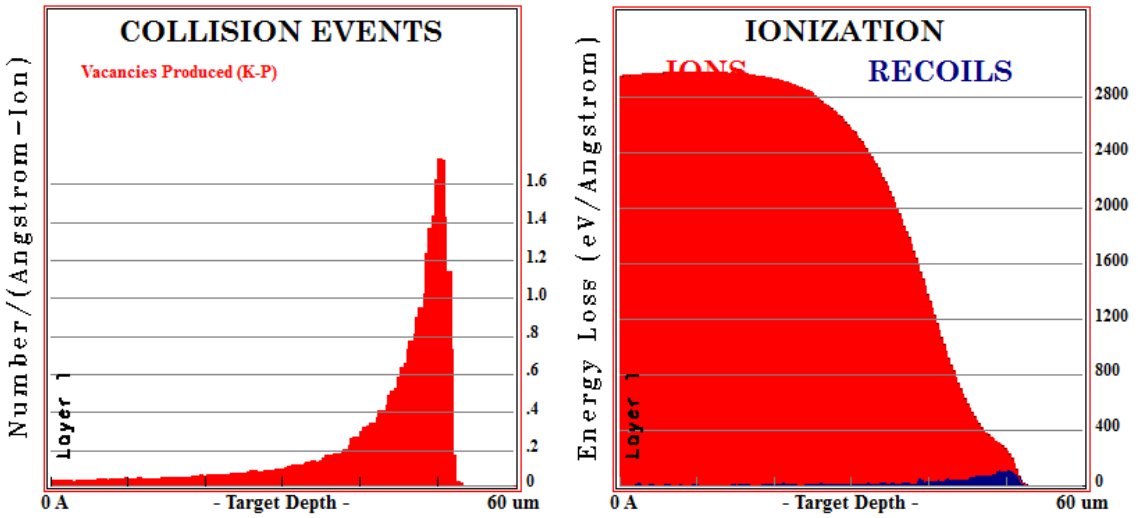

Figure 25. TRIM calculation for the distribution of vacancies (left) and energy loss (right) of GaP irradiated with 1.16 GeV Au ions.

4.3 X-ray Photoelectron Spectroscopy (XPS)

The XPS spectra were recorded in the range of C 1s, O 1s, Ga 3d, and P 2p core level photoemission peaks. Under exposure to the ambient conditions, the surface of type III-V semiconductor materials are usually covered with native oxide layers. Since our samples are undoped GaP single crystals, it is required to verify that these layers are due to surface contamination and do not exist inside the bulk. Therefore, *in-situ* Ar^+ ion gun were implemented to clean the surface of the samples.

The XPS spectra of the virgin sample before and after applying surface cleaning treatment in Ga 3d and P 2p are shown in Figure 26 and Figure 27, respectively. The peak position for Ga 3d, P $2p_{3/2}$ and P $2p_{1/2}$ are at ~19.1 eV, ~128.6 eV and at ~129.5 eV, respectively. Ga 3d spectrum was not fitted to its components (Ga $3d_{5/2}$ and Ga $3d_{3/2}$) because they overlap in binding energy. One can see that without using Ar^+ ion cleaning that both Ga_2O_3 peak at ~20.6 eV and P_2O_5 at ~133.6 eV are appearing in the spectra as native oxides for

gallium and phosphorus, respectively [62]. Furthermore, we observe the removal of the signal both from Ga_2O_3 and P_2O_5 by applying 3 keV Ar^+ etching for 30 s, which confirms the purity of the single crystal bulk.

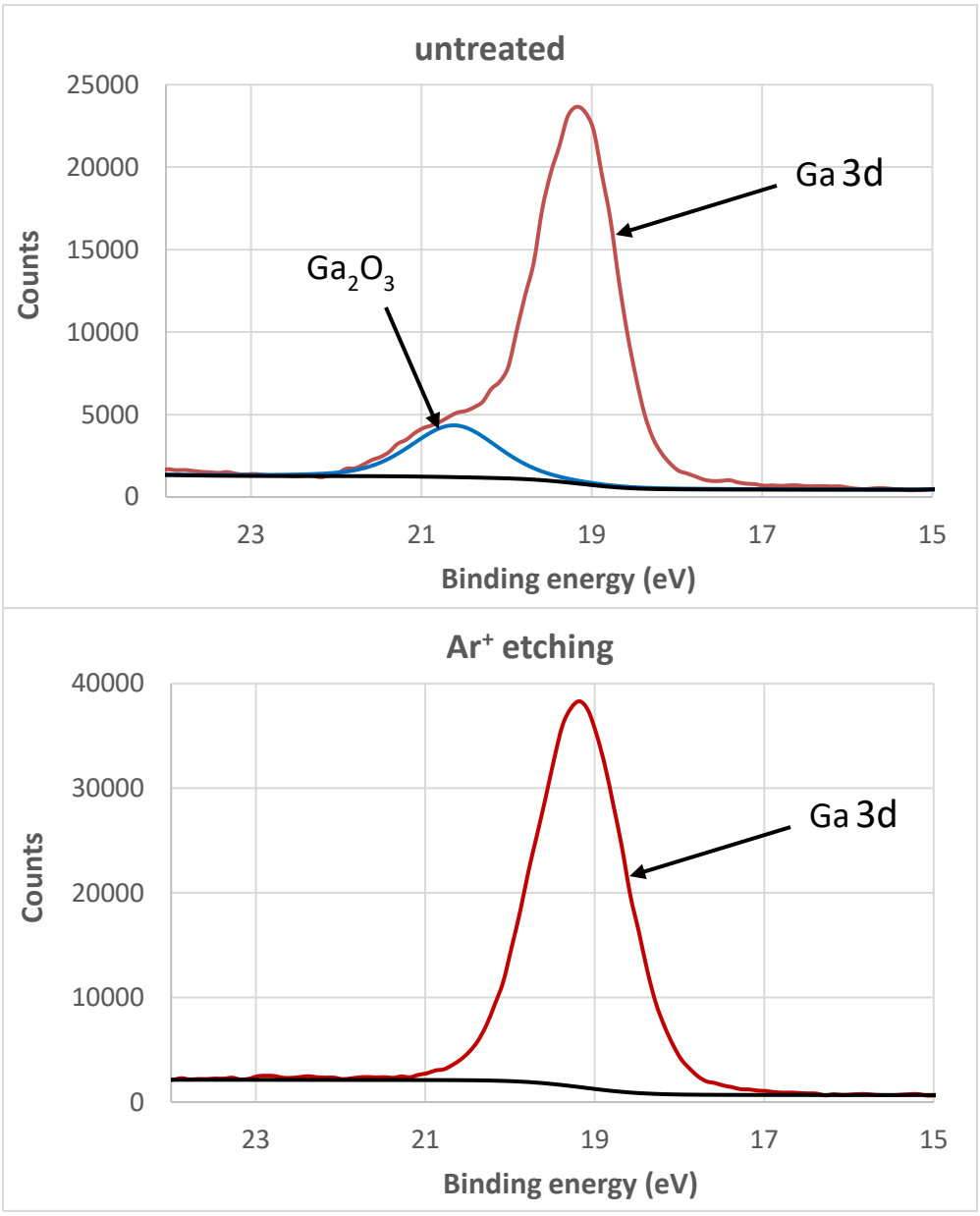

Figure 26. XPS spectrum in the Ga 3d region of the virgin sample without surface cleaning treatment (top) and after etching with Ar^+ ions (bottom).

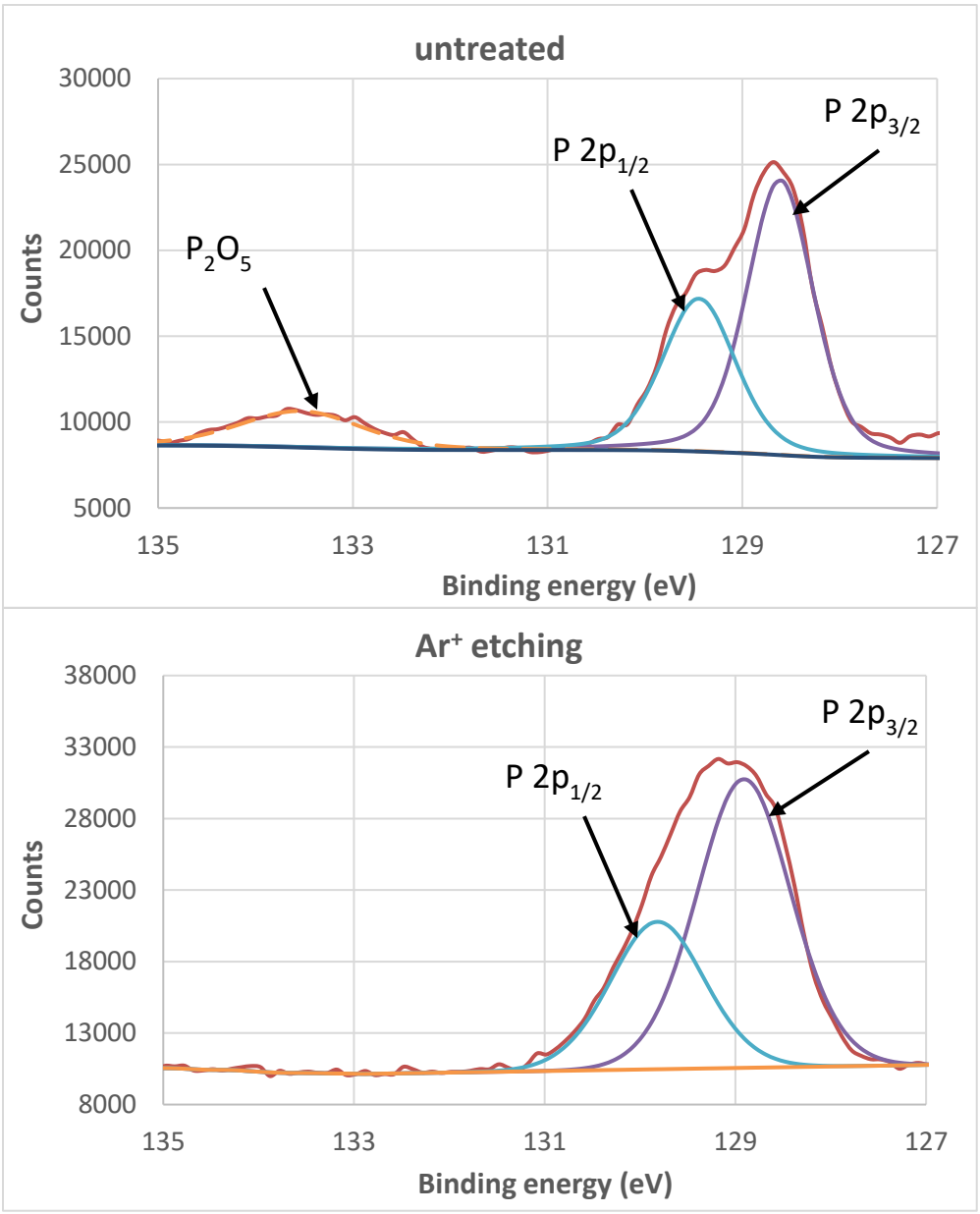

Figure 27. XPS spectrum in the P 2p region of the virgin sample without surface cleaning treatment (top) and after etching with Ar^+ ions (bottom).

4.3.1 Peak Position Analysis

The peaks positions of the Ga 3d and P 2p from the virgin and irradiated samples were investigated to analyze the effect of ion irradiation in GaP surface structure. This is done mainly by plotting them as a function of the electronic energy loss and ion fluence. The results show no systematical change in the peak position due to ion irradiation for both Ga 3d and P 2p peaks positions, as shown in Figures 28 to 31.

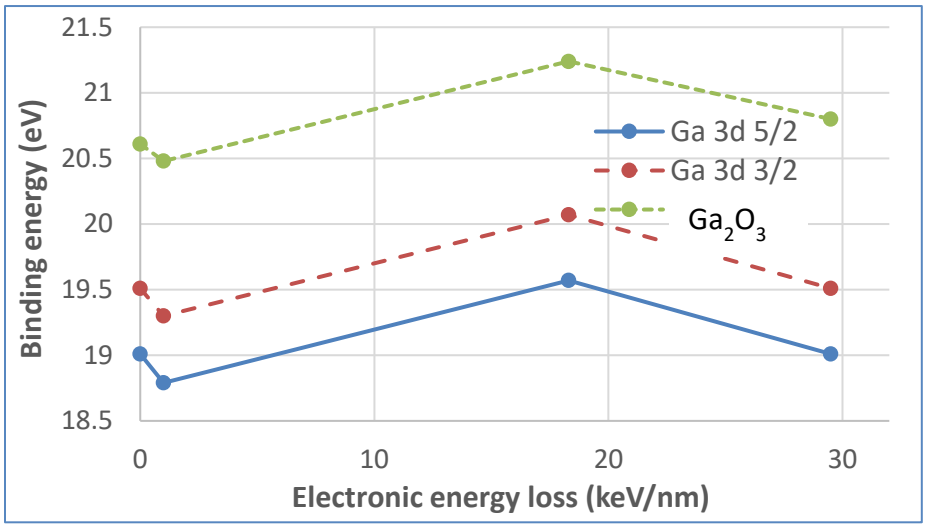

Figure 28. XPS peak position of Ga 3d versus electronic energy loss.

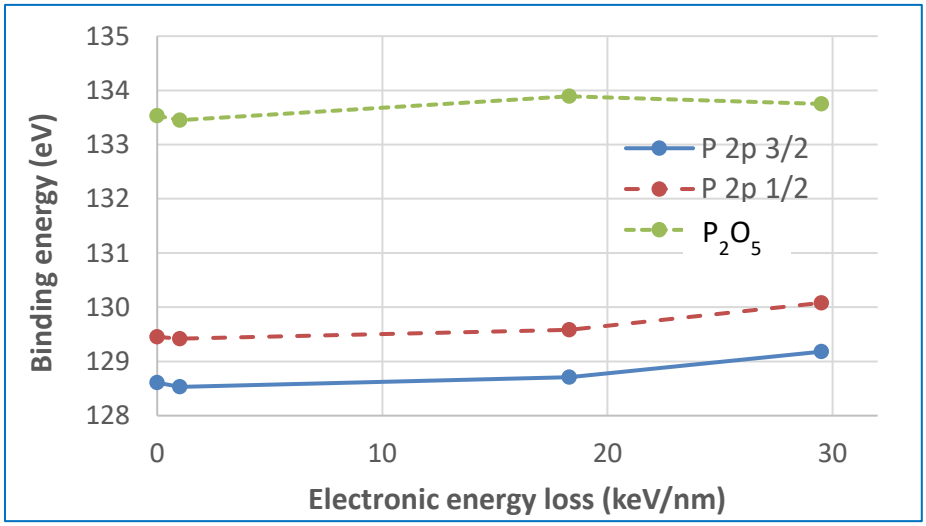

Figure 29. XPS peak position of P 2p versus electronic energy loss.

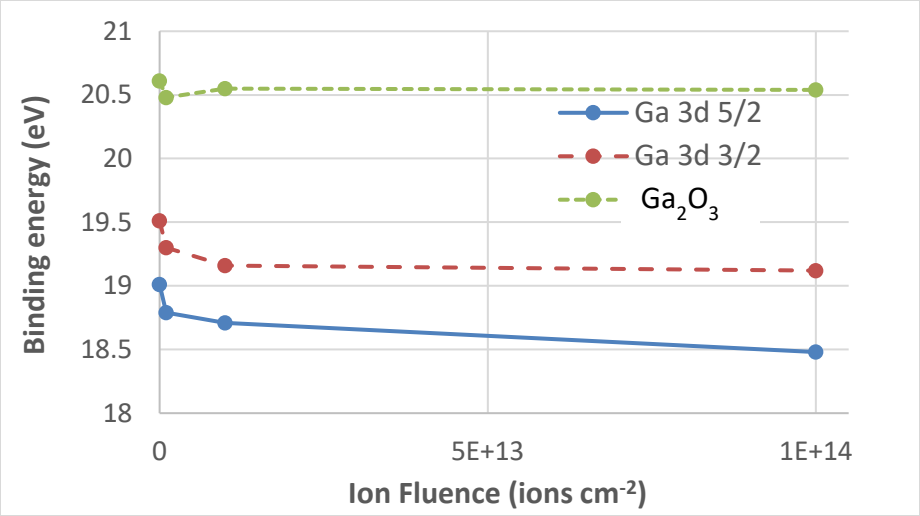

Figure 30. XPS peak position of Ga 3d versus ion fluence.

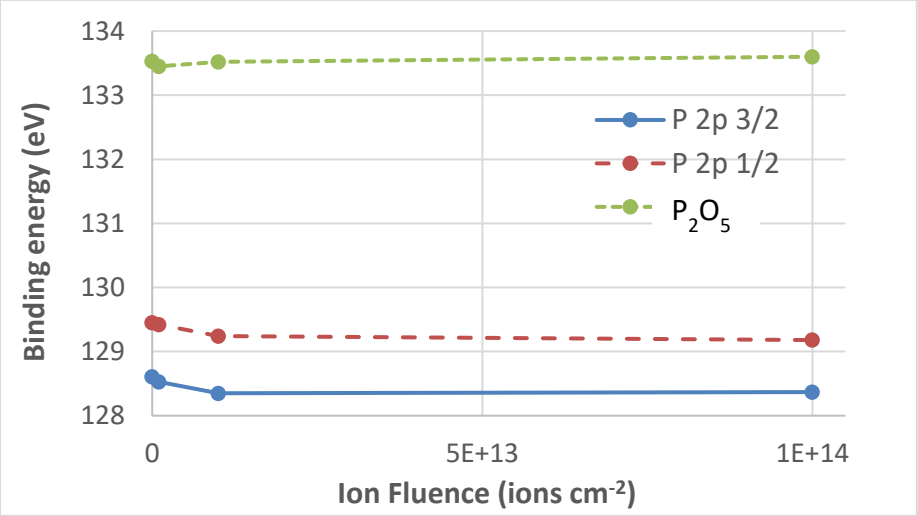

Figure 31. XPS peak position of P 2p versus ion fluence.

4.3.2 Peak Intensity Analysis

To study the effect of ion irradiation in GaP single crystals, the peak intensity of Ga 3d and P 2p from the virgin and irradiated samples were also investigated by plotting them as a function of electronic energy loss and ion fluence. The results also show no systematic change induced by ion irradiation in the peak intensity, as shown in Figures 32 and 33.

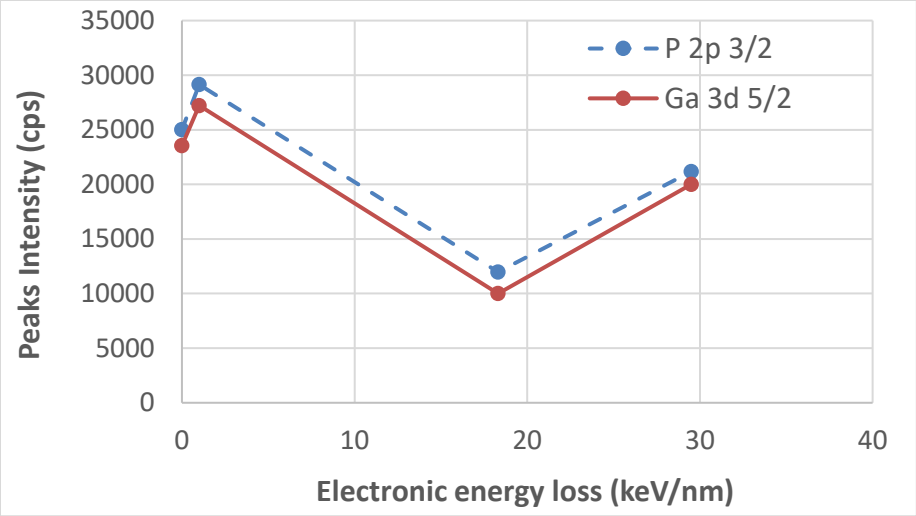

Figure 32. XPS peaks intensity of Ga 3d and P 2p versus electronic energy loss.

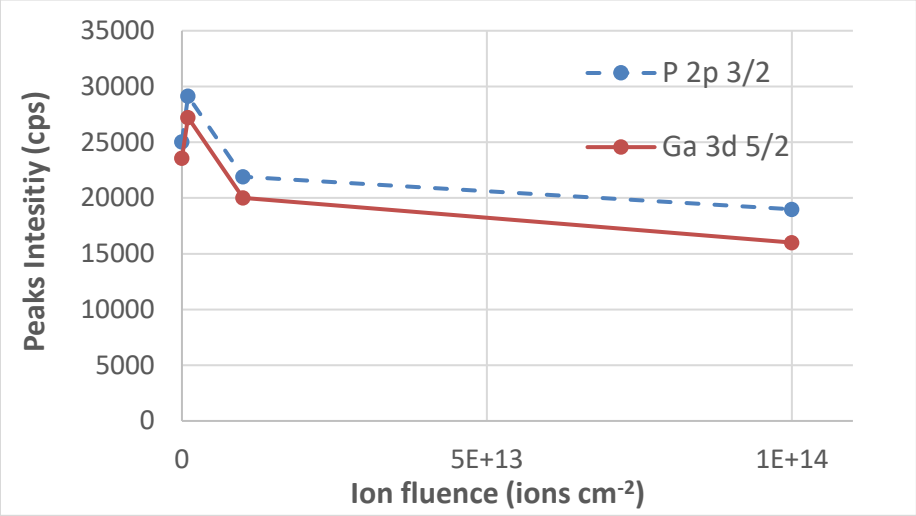

Figure 33. XPS peaks intensity of Ga 3d and P 2p versus ion fluence.

4.4 UV-Visible Spectroscopy

4.4.1 Transmission Spectrum

UV-visible spectroscopy measurements were performed for the virgin and various ion irradiated GaP single crystals. The measured spectra showed interesting results based on their evolution as a function of ion beam parameters. The first observation is the red shift of the absorption edge in comparison to the one observed for the virgin sample indicating a reduction of the band gap [16, 17]. Furthermore, we observed a decrease of the intensity of transmission spectra at the same wavelength, as a function of ion fluence (Figures 34 – 38) and ion energy loss (Figures 39 and 40). This is argued to the present of SHI induced defects in the GaP sample that absorb the photon energy, reducing the transmission [13]. The number of the induced defects is increasing as a function of ion fluence and ion energy loss.

It is important to note that the irradiation with SHI resulted in color change of the GaP crystals. This effect is even more pronounce for the samples irradiated with higher ion fluence and electronic energy loss.

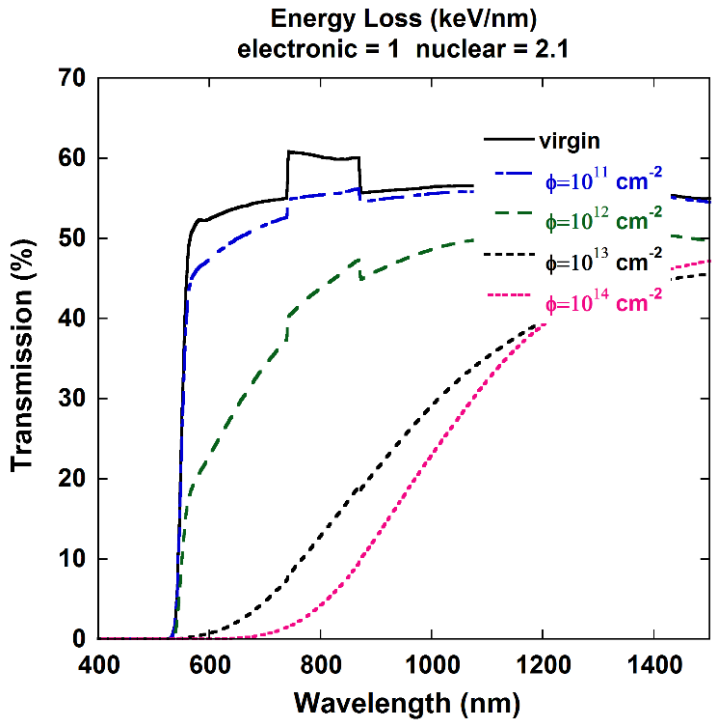

Figure 34. Transmission spectrum of GaP samples irradiated with 1 MeV iodine ions of various fluences.

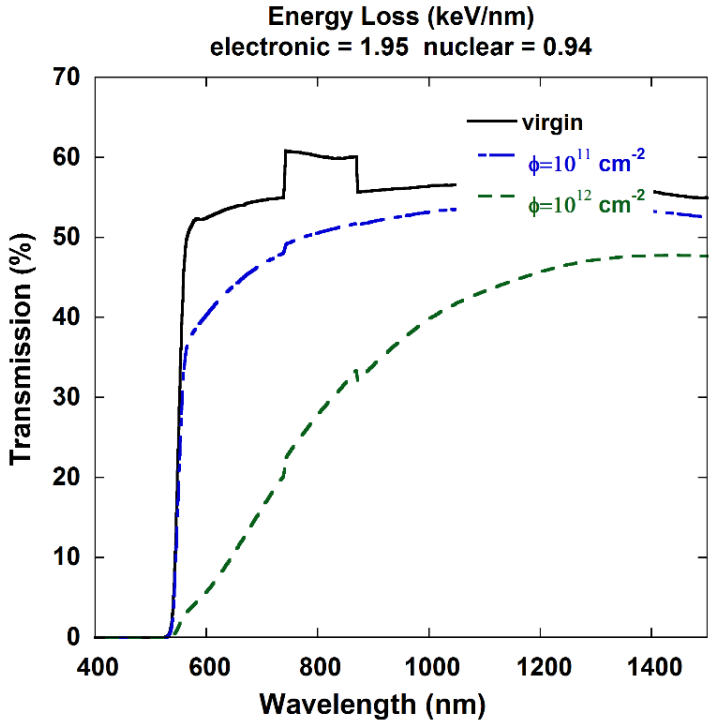

Figure 35. Transmission spectrum of GaP samples irradiated with 6 MeV iodine ions of various fluences

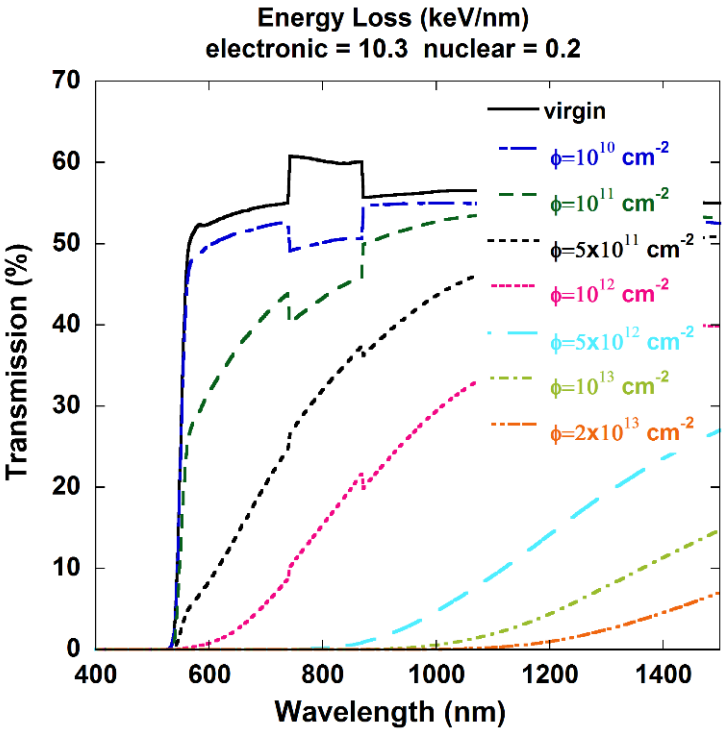

Figure 36. Transmission spectrum of GaP samples irradiated with 54 MeV iodine ions of various fluences

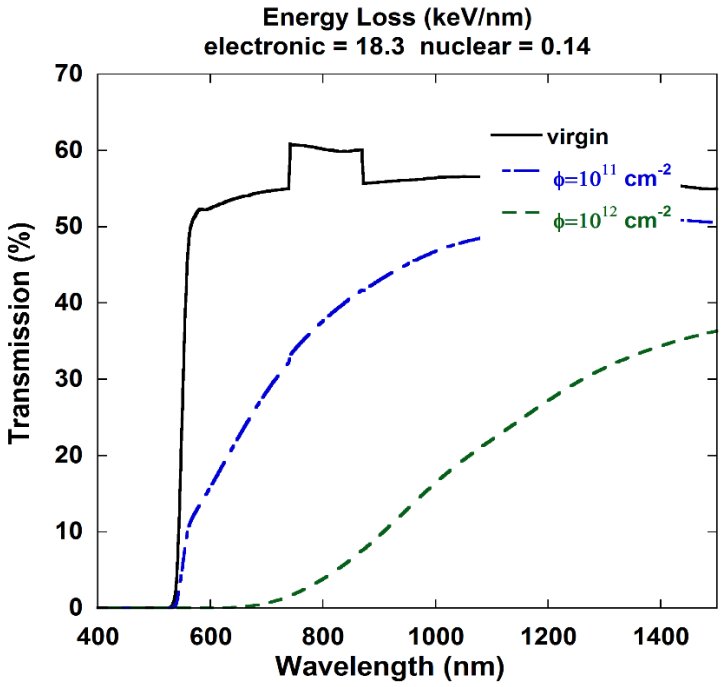

Figure 37. Transmission spectrum of GaP samples irradiated with 240 MeV gold ions of various fluences.

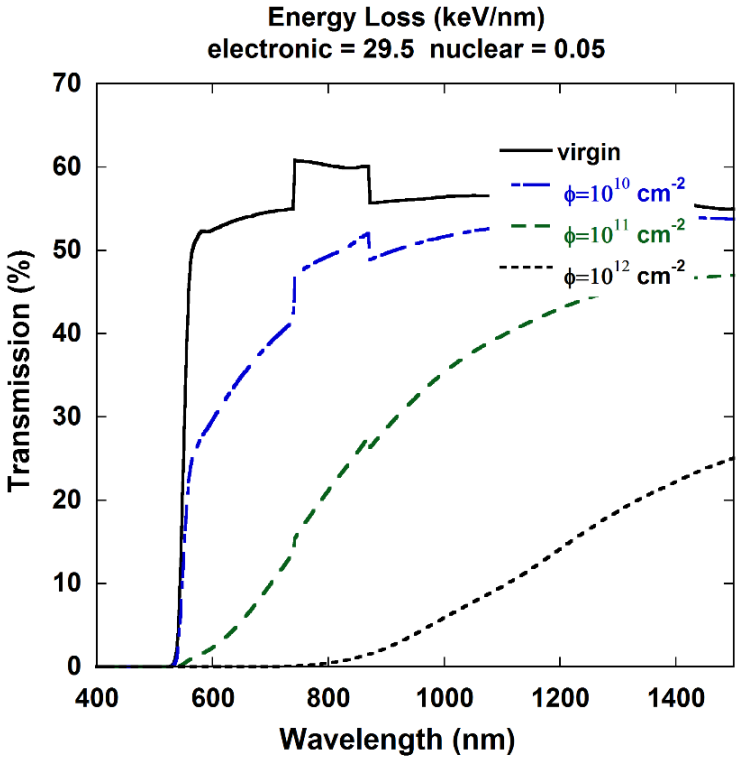

Figure 38. Transmission spectrum of GaP samples irradiated with 1.16 GeV gold ions of various fluences.

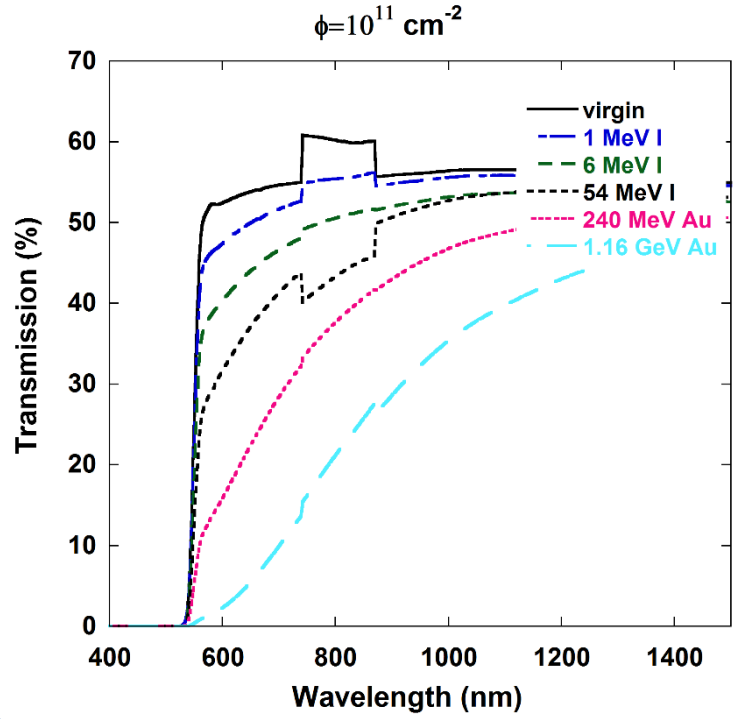

Figure 39. Transmission spectrum of GaP samples irradiated with 10^{12} ions cm^{-2} of various kinetic energies.

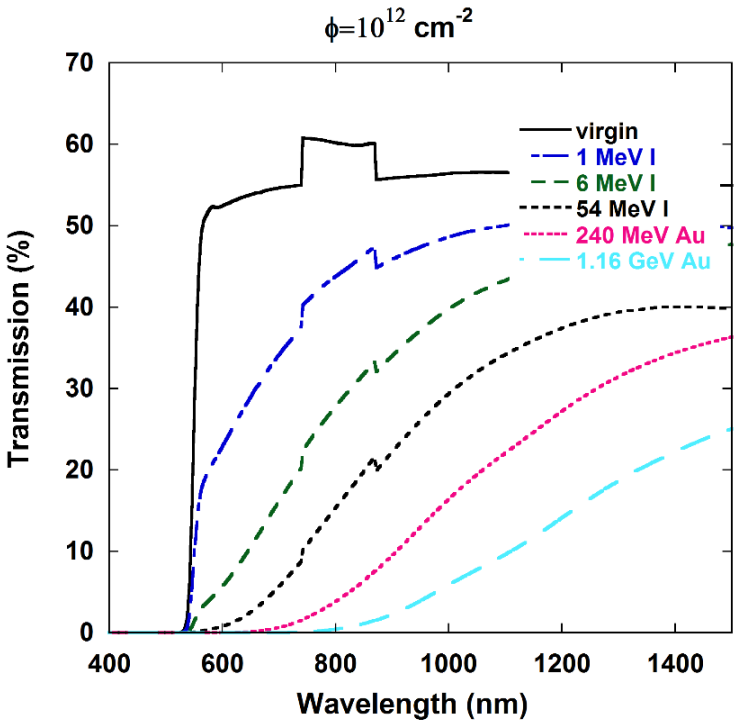

Figure 40. Transmission spectrum of GaP samples irradiated with 10^{12} ions cm^{-2} of various kinetic energies.

4.4.2 Optical band gap estimation

The energy optical band gap estimation was performed using Tauc's plot for the indirect band to band transitions obtained from the relation [63]

$$\alpha h\nu = C\left(E - E_g\right)^2 \tag{17}$$

where α is the absorption coefficient, E is the photon energy, C is a constant related to the specific features of the band structure and E_g is the optical band gap. The values of band gap energy were estimated by plotting the $(\alpha h\nu)^{1/2}$ vs photon energy, and taking the intersection of the linear fit of the curve with x-axis.

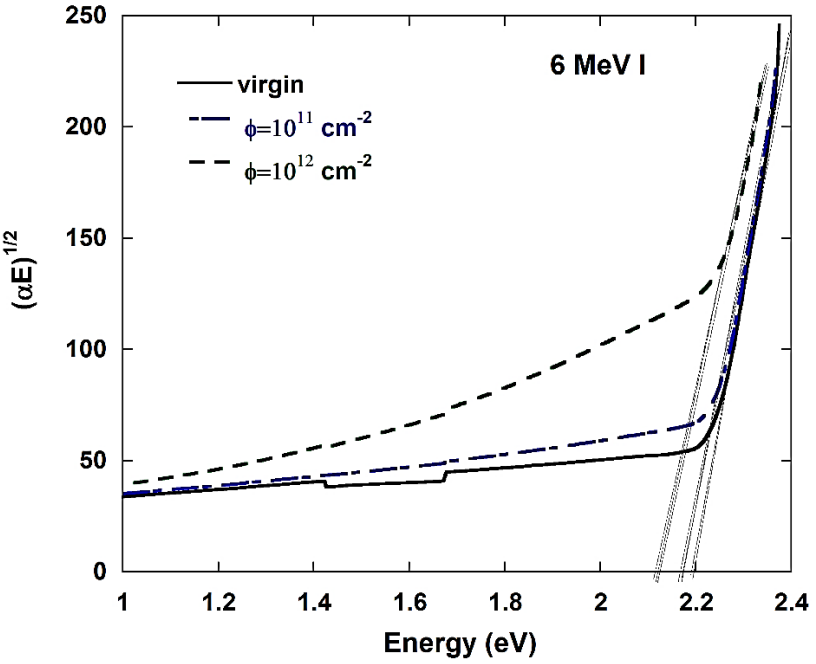

Figure 41. $(\alpha h\nu)^{1/2}$ versus photon energy of GaP irradiated with 6 MeV iodine ions of various fluences.

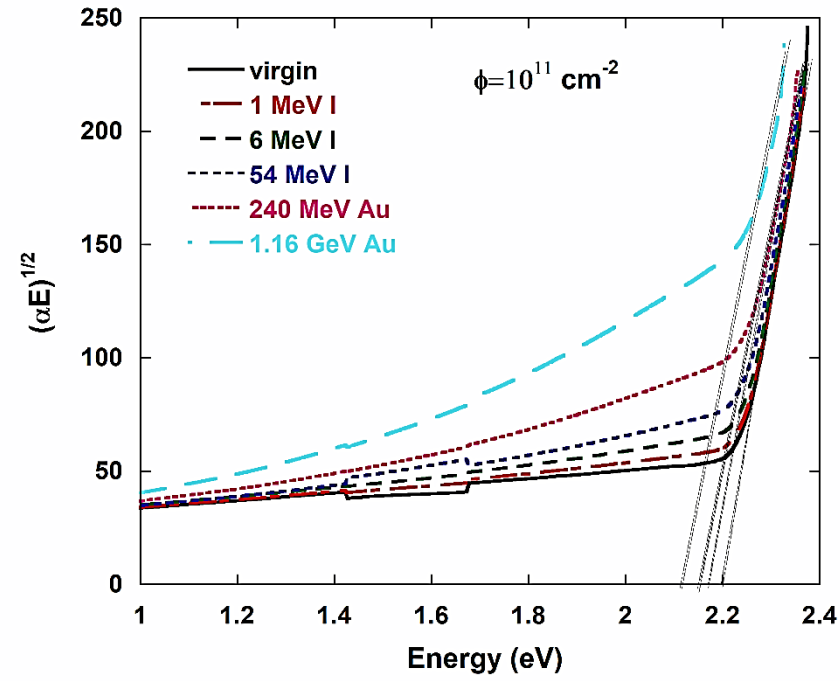

Figure 42. $(\alpha h\nu)^{1/2}$ versus photon energy of GaP irradiated with 10^{12} ions cm^{-2} of various energies.

The change in the band structure may arise from the band tailing effect due to the SHI induced defects. The defects produced in the vicinity of ion tracks contribute to the

formation of localized states near the band edges which reduce the band gap [15], [64]. The width of the tail of the localized states within the band gap is called Urbach tail, which is estimated by

$$E_u = E_g^{virgin} - E_g^{irr} \tag{18}$$

where E_g^{virgin} is the band gap of the virgin sample and E_g^{irr} is the band gap of the irradiated samples. The evolutions of Urbach tail as a function of ion fluence and electronic energy loss are shown in Figure 43 and Figure 44, respectively. It can be seen that for the same ion fluence, the larger electronic energy loss results in longer Urbach tail. Moreover, for the ions exhibiting the same electronic energy loss, longer Urbach tail was observed by increasing ion fluence.

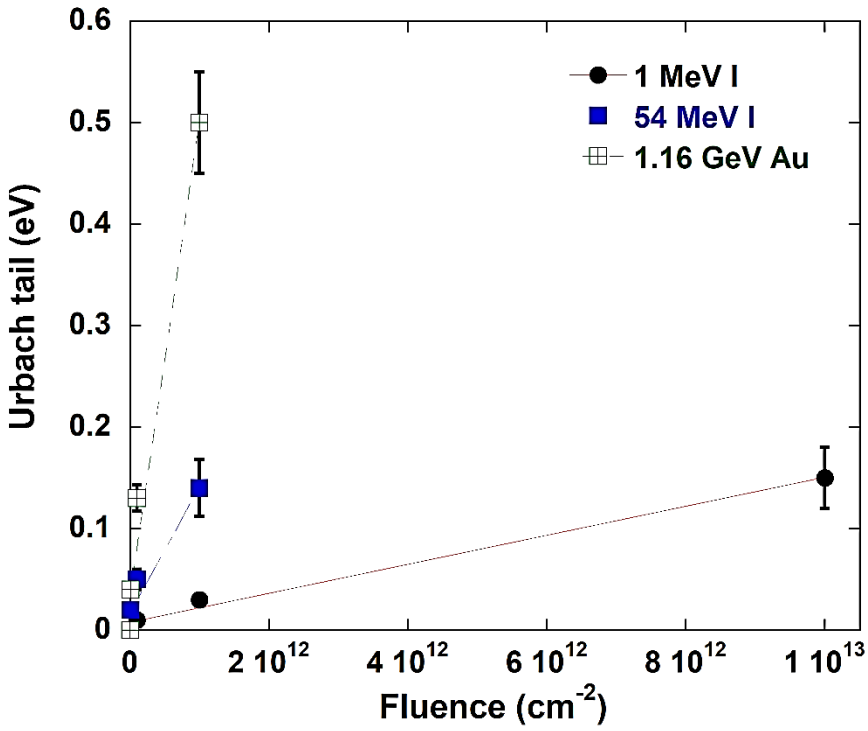

Figure 43. Urbach tail versus ion fluence of GaP irradiated with various kinetic energies. The lines are guides to the eye.

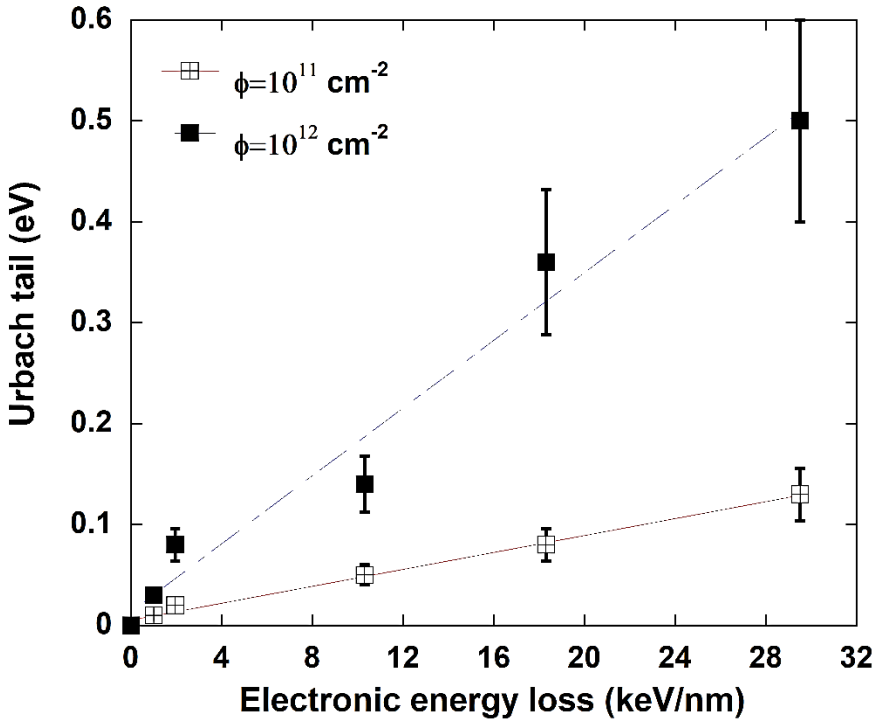

Figure 44. Urbach tail vs electronic energy loss of GaP irradiated with 10^{11} and 10^{12} ions cm^{-2}.

Band gap reduction can also be ascribed to the formation of larger sized particles in the material [16, 65]. It is worth mentioning that empirical relation between the band gap and lattice constant in cubic semiconductor also states that band gap is directly proportional to the inverse of squared lattice constant [66]. This relation has been found to hold reasonably well for a wide range of semiconductor with NaCl structure.

4.4.3 Transmission and Relative Band Gap: Ion Fluence Dependence

The damage cross-section σ can be approximated from the Poisson's distribution which describes the evolution of the transmission as a function of the applied ion fluence [5, 67]

$$T(\Phi) = T(\infty)\left(1 - \sum_{k=0}^{n-1} \frac{(\sigma\Phi)^k}{k!} \exp(-\sigma\Phi)\right) \tag{19}$$

where $T(\Phi)$ and $T(\infty)$ are the transmission at finite fluence Φ and saturation, respectively. σ is the cross section of the cylinder around the ion path where matter undergoes transformation, and n is the minimum number of required ion impacts in order to transform this cylindrical zone to the final state.

To study the transmission variation as a function of ion fluence, the values of transmission were estimated at wavelength=1000 nm and plotted as a function of ion fluence. The fit of Equation 19 to the transmission data is depicted in Figure 45 resulting the following values:

- $\sigma = 3.7 \times 10^{-13}$ cm^2 and n=3 for 1 MeV I irradiation,

- $\sigma = 7.1 \times 10^{-13}$ cm^2 and n=2 for 54 MeV I irradiation, and,

- $\sigma = 5.4 \times 10^{-12}$ cm^2 and n=1 for 1.16 GeV Au irradiation.

One can see that the damage cross section increases with the electronic energy loss which is in agreement with other works using other materials [36, 67, 68]. On the other hand, the number of ion impact required for inducing the observed effect is decreasing as a function of electronic energy loss.

To study the change in optical band gap induced by MeV-GeV ion irradiation, we estimated the relative band gap in order to see the change of band gap as a function of ion beam parameters. Relative band gap of each sample was calculated by normalizing the estimated band gap for the ion irradiated samples to the one estimated for the virgin sample in percentage. The dependence of relative band gap of GaP samples on ion fluence is shown in Figure 46. One can see that the band gap decreases as a function of ion fluence for ions

having the same kinetic energy. The data are fitted using Equation 19 for single ion impact resulting in the following values:

-$\sigma = 1.4 \times 10^{-14}$ cm^2 for 1 MeV I irradiation,

-$\sigma = 1.1 \times 10^{-13}$ cm^2 for 54 MeV I irradiation, and

-$\sigma = 5.7 \times 10^{-13}$ cm^2 for 1.16 GeV Au irradiation.

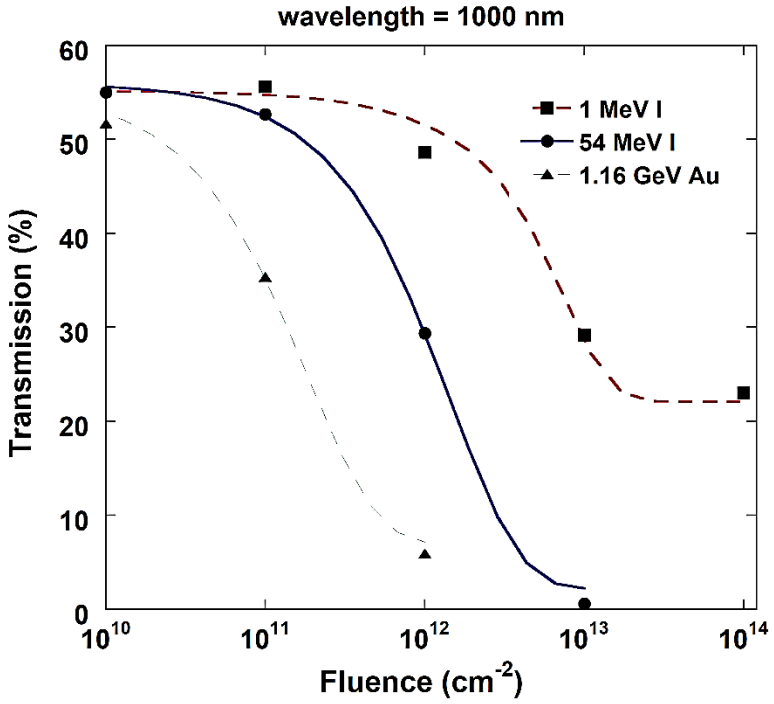

Figure 45. Transmission of irradiated GaP samples at $\lambda = 1000$ nm versus ion fluence of various ion kinetic energies.

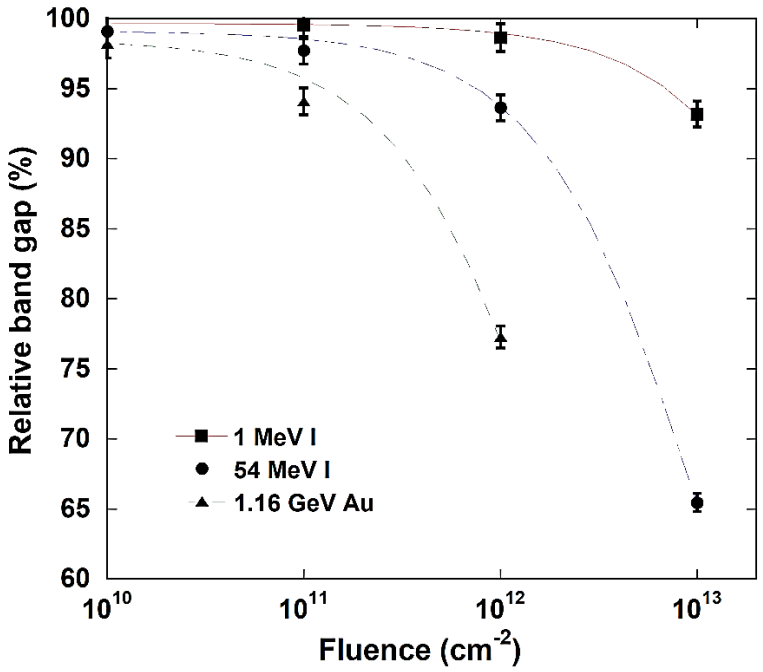

Figure 46. Relative band gap values of irradiated GaP samples versus ion fluence of various ion kinetic energies.

4.4.4 Transmission and Relative Band Gap: Electronic Energy Loss Dependence

To study the evolution of transmission as a function of electronic energy loss, the values of transmission were estimated at wavelength=1000 nm and plotted as function of electronic energy loss at constant ion fluence (see Figure 47). The dependence of the relative band gap of the irradiated GaP samples on the electronic energy loss is shown in Figure 48. One can see that both relative band gap and transmission decrease as a function of electronic energy loss at constant ion fluence.

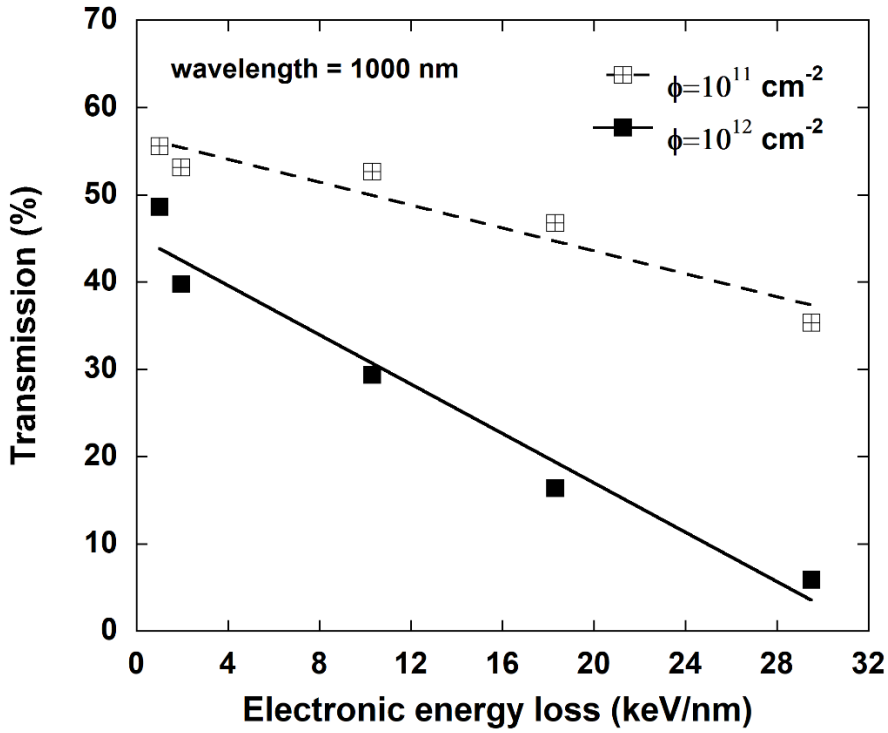

Figure 47. Transmission at λ=1000 nm of GaP irradiated with 10^{11} and 10^{12} ions cm^{-2} versus electronic energy loss.

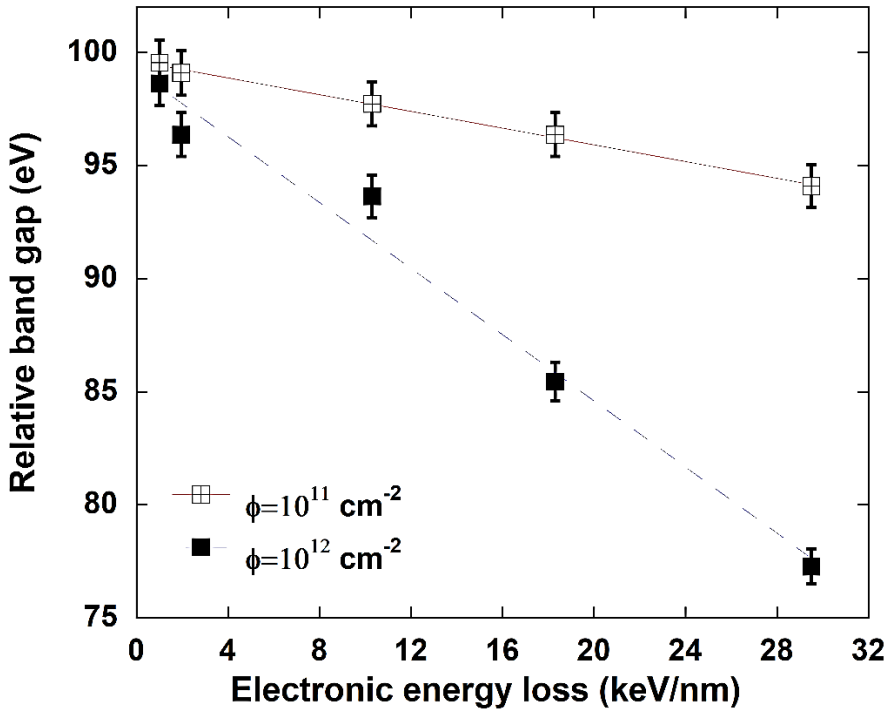

Figure 48. Relative band gap of GaP irradiated with 10^{11} and 10^{12} ions cm^{-2} versus electronic energy loss.

CHAPTER 5

CONCLUSIONS

In this work, we have investigated the modification induced by slow highly charged ions (HCI) and swift heavy ions (SHI) in GaP single crystals. For HCI, the samples were irradiated with 114 keV Xe^{q+} (q=33-40) from the EBIT facility of HZDR (Dresden, Germany). The irradiation with SHI was done at the 6 MV tandem accelerator facility of HZDR using 1-54 MeV I ions, and at the UNILAC facility of GSI (Darmstadt, Germany) using 240 MeV-1.16 GeV Au ions.

AFM measurements showed that the irradiation of GaP with SHI can result in the formation of surface nanohillocks. For a single ion impact, the electronic energy loss threshold for creation of these nanostructures is found to be between 10.3 and 18.3 keV/nm. In contrast, such nanostructures could not be created by irradiation with 114 keV highly charged xenon ions even for the ones carrying the highest available charge state ($q = 40$ of potential energy ~ 38.5 keV).

Formation of amorphous layer in GaP crystals was observed by means of Rutherford backscattering spectrometry under irradiation with 1 MeV iodine of fluence $\Phi = 1 \times 10^{14}$ ions cm^{-2}. The ion-induced amorphization was not observed after irradiation with 54 MeV iodine and 1.16 GeV gold ions in spite of the huge electronic energy deposition suggesting that in GaP amorphization could only be achieved based on nuclear energy deposition via elastic collisions of ions with the lattice atom.

The evolution of optical transmission spectra as a function of ion beam parameters showed interestingly that the SHI irradiated GaP crystals exhibit a red shift of the absorption edge in comparison to the one observed for the virgin sample. Moreover, a decrease in the band gap as a function of ion energy loss and ion fluence was observed. In addition, we observed a decrease in transmission of UV-Vis spectra, at the same wavelength, as a function of ion energy loss and ion fluence. This decrease is attributed to the presence of SHI induced defects.

The demonstration of tuning the modification of the optical properties, by swift heavy ions, is of high importance for the applications of GaP (e.g. in electronic devices).

References

[1] D. K. Avasthi and G. K. Mehta, *Swift Heavy Ions for Materials Engineering and Nanostructuring*. India: Springer, 2011.

[2] D. K. Avasthi, "Nanostructuring by Energetic Ion Beams," *Hyperfine Interact.*, vol. 160, pp. 95–106, 2005.

[3] M. Toulemonde, W. Assmann, C. Trautmann, and F. Grüner, "Jetlike Component in Sputtering of LiF Induced by Swift Heavy Ions," *Phys. Rev. Lett.*, vol. 88, no. 5, pp. 3–6, 2002.

[4] M. Karlušić, R. Kozubek, H. Lebius, B. Ban-d'Etat, R. A. Wilhelm, M. Buljan, Z. Siketić, F. Scholz, T. Meisch, M. Jakšić, S. Bernstorff, M. Schleberger, and B. Šantić, "Response of GaN to energetic ion irradiation: conditions for ion track formation," *J. Phys. D. Appl. Phys.*, vol. 48, no. 32, p. 325304, 2015.

[5] J. F. Gibbons, "Ion implantation in semiconductors-Part II Damage production and annealing," *Proc. IEEE*, vol. 60, no. 9, pp. 1062–1095, 1972.

[6] A. Kamarou, W. Wesch, E. Wendler, A. Undisz, and M. Rettenmayr, "Swift heavy ion irradiation of InP : Thermal spike modeling of track formation," *Phys. Rev. B*, vol. 73, no. 18, p. 18107, 2006.

[7] A. V Solov'yov, E. Surdutovich, E. Scifoni, I. Mishustin, and W. Greiner, "Physics of ion beam cancer therapy : a multi-scale approach," *Phys. Rev. E*, vol. 79, no. 1, pp. 1–18, 2009.

[8] D. K. Avasthi, "Modification and characterisation of materials by swift heavy ions," *Def. Sci. J.*, vol. 59, no. 4, pp. 401–412, 2009.

[9] A. S. El-Said, W. Meissl, M. C. Simon, J. R. Crespo Lopez-Urrutia, I. C. Gebeshuber, M. Lang, H. P. Winter, J. Ullrich, and F. Aumayr, "Surface nanostructures induced by slow highly charged ions on CaF 2 single crystals," *Nucl. Instruments Methods Phys. Res. Sect. B Beam Interact. with Mater. Atoms*, vol. 256, pp. 346–349, 2007.

[10] A. S. El-Said, R. Heller, R. Ritter, G. Wachter, S. Facsko, C. Lemell, J. Burgdorfer, and F. Aumayr, "Nanostructuring CaF2 surfaces with slow highly charged ions," *J. Phys. Conf. Ser.*, vol. 488, no. 1, p. 012002, 2014.

[11] S. Facsko, R. Heller, A. S. El-Said, W. Meissl, and F. Aumayr, "Surface nanostructures by single highly charged ions," *J. Phys. Condens. Matter*, vol. 21, no. 22, p. 224012, 2009.

[12] Y. Zhu, Z. Wang, J. Sun, C. Yao, K. Wei, J. Gou, Y. Ma, T. Shen, L. Pang, and Y. Sheng, "Modification of Optical Band-Gap of Si Films After Ion Irradiation,"

Plasma Sci. Technol., vol. 14, no. 7, pp. 632–635, 2012.

[13] R. L. Dubey and S. K. Dubey, "Surface Modification and Irradiation Strength of InP and GaP," *Int. J. Chem. Phys. Sci.*, vol. 5, no. 2016, pp. 51–58, 2016.

[14] R. Kumaravel, K. Ramamurthi, I. Sulania, K. Asokan, D. Kanjilal, D. K. Avasti, and P. K. Kulria, "Effect of swift heavy ion irradiation on structural , optical and electrical properties of spray deposited CdO thin films," *Radiat. Phys. Chem.*, vol. 80, no. 3, pp. 435–439, 2011.

[15] S. Rani, N. K. Puri, S. C. Roy, M. C. Bhatnagar, and D. Kanjilal, "Effect of swift heavy ion irradiation on structure, optical, and gas sensing properties of SnO2 thin films," *Nucl. Instruments Methods Phys. Res. Sect. B Beam Interact. with Mater. Atoms*, vol. 266, no. 9, pp. 1987–1992, 2008.

[16] R. Sivakumar, C. Sanjeeviraja, M. Jayachandran, R. Gopalakrishnan, S. N. Sarangi, D. Paramanik, and T. Som, "MeV N+-ion irradiation effects on α-MoO3 thin films," *J. Appl. Phys.*, vol. 101, no. 3, pp. 1–6, 2007.

[17] S. Sorieul, J.-M. Costantini, L. Gosmain, G. Calas, J.-J. Grob, and L. Thomé, "Study of damage in ion-irradiated α-SiC by optical spectroscopy," *J. Phys. Condens. Matter*, vol. 18, no. 37, pp. 8493–8502, 2006.

[18] R. Kumar, S. A. Ali, A. K. Mahur, H. S. Virk, F. Singh, S. A. Khan, D. K. Avasthi, and R. Prasad, "Study of optical band gap and carbonaceous clusters in swift heavy ion irradiated polymers with UV – Vis spectroscopy," *Nucl. Instruments Methods Phys. Res. Sect. B Beam Interact. with Mater. Atoms*, vol. 266, pp. 1788–1792, 2008.

[19] A. Semwal, A. Negi, R. G. Sonkawade, J. M. S. Rana, and R. C. Ramola, "Effect of swift heavy ion irradiation on optical and structural properties of polysulphones polymer films," *Indian J. Pure Appl. Phys.*, vol. 48, pp. 496–499, 2010.

[20] M. Levalois and P. Marie, "Damage induced in semiconductors by swift heavy ion irradiation," *Nucl. Instruments Methods Phys. Res. Sect. B Beam Interact. with Mater. Atoms*, vol. 156, pp. 64–71, 1999.

[21] W. Wesch, A. Kamarou, and E. Wendler, "Effect of high electronic energy deposition in semiconductors," *Nucl. Instruments Methods Phys. Res. Sect. B Beam Interact. with Mater. Atoms*, vol. 225, pp. 111–128, 2004.

[22] A. S. El-Said, M. Cranney, N. Ishikawa, A. Iwase, R. Neumann, K. Schwartz, M. Toulemonde, and C. Trautmann, "Study of heavy-ion induced modifications in BaF 2 and LaF 3 single crystals," *Nucl. Instruments Methods Phys. Res. Sect. B Beam Interact. with Mater. Atoms*, vol. 218, pp. 492–497, 2004.

[23] J. F. Ziegler, J. Biersack, and U. and Littmark, *The Stopping and Range of Ions in Matter*. Oxford: Pergamon Press, 1985.

[24] J. Lindhard, M. Scharf, and H. E. Schiott, "Range concepts and heavy ion ranges," *Mat. Fys. Medd. Dan. Vid. Selsk*, vol. 33, no. 25, pp. 1–42, 1963.

[25] F. Bloch, “Zur Bremsung rasch bewegter Teilchen beim Durchgang durch Materie,” *Ann. Phys.*, vol. 408, no. 3, pp. 285–320, 1933.

[26] L. A. Giannuzzi, B. I. Prenitzer, and B. W. Kempshall, *Introduction to Focused Ion Beams*. Orlando: Springer, 2005.

[27] I. Bogdanovic-Radovic, M. Buljan, M. Karlušić, N. Skukan, I. Bozicevic, M. Jakšić, and N. Radic, “Conditions for formation of germanium quantum dots in amorphous matrices by MeV ions :Comparison with standard thermal annealing,” *Phys. Rev. B*, vol. 86, no. 16, p. 165316, 2012.

[28] A. Meftah, F. Brisard, J. M. Constantini, M. Hage-Ali, J. P. Stoquert, F. Studer, and M. Toulemonde, “Swift heavy ions in magnetic insulators: A damage-cross-section velocity effect,” *Phys. Rev. B*, vol. 48, no. 2, pp. 920–925, 1993.

[29] A. S. El-Said, R. A. Wilhelm, R. Heller, S. Facsko, C. Trautmann, and F. Aumayr, “Surface nanostructuring of SrTiO 3 single crystals by slow highly charged ions and swift heavy ions,” *Nucl. Instruments Methods Phys. Res. Sect. B Beam Interact. with Mater. Atoms*, vol. 269, no. 11, pp. 1234–1237, 2011.

[30] H. P. Winter, S. Lederer, F. Aumayr, and H. Winter, “Electron Emission for Grazing Slow Atom and Ion Impact on Monocrystalline Metal and Insulator Surfaces,” *Phys. Scr.*, vol. 72, pp. 12–21, 2005.

[31] R. A. Wilhelm, A. S. El-said, F. Krok, R. Heller, E. Gruber, F. Aumayr, and S. Facsko, “Highly charged ion induced nanostructures at surfaces by strong electronic excitations,” *Prog. Surf. Sci.*, vol. 90, no. 3, pp. 377–395, 2015.

[32] Z. G. Wang, C. Dufour, E. Paumier, and M. Toulemonde, “The Se sensitivity of metals under swift-heavy-ion irradiation : a transient thermal process,” *J. Phys. Condens. Matter*, vol. 6, no. 34, pp. 6733–6750, 1994.

[33] A. S. El-said, “Heavy Ion-Induced Damage in Ionic Fluoride Single Crystals,” Ruperto-Carola University of Heidelberg, Germany, 2004.

[34] W. Wesch, A. Kamarou, E. Wendler, A. Undisz, and M. Rettenmayr, “Effect of high electronic excitation in swift heavy ion irradiated semiconductors,” *Nucl. Instruments Methods Phys. Res. Sect. B Beam Interact. with Mater. Atoms*, vol. 257, pp. 283–286, 2007.

[35] J. Zhang, M. Lang, R. C. Ewing, R. Devanathan, W. J. Weber, and M. Toulemonde, “Nanoscale phase transitions under extreme conditions within an ion track,” *J. Mater. Res.*, vol. 25, no. 7, pp. 1344–1351, 2010.

[36] A. Kamarou, W. Wesch, E. Wendler, A. Undisz, and M. Rettenmayr, “Radiation damage formation in InP, InSb, GaAs, GaP, Ge, and Si due to fast ions,” *Phys. Rev. B - Condens. Matter Mater. Phys.*, vol. 78, no. 5, p. 54111, 2008.

[37] A. Colder, O. Marty, B. Canut, M. Levalois, P. Marie, X. Portier, S. Ramos, and M. Toulemonde, “Latent track formation in germanium irradiated with 20, 30 and 40

mev fullerenes in the electronic regime," *Nucl. Instruments Methods Phys. Res. Sect. B Beam Interact. with Mater. Atoms*, vol. 174, no. 4, pp. 491–498, 2001.

[38] M. Karlušić, S. Fazinic, S. Zdravko, T. Tadic, D. D. Cosic, I. Bozicevic, I. Zamboni, M. Jakšić, and M. Schleberger, "Monitoring Ion Track Formation Using In Situ RBS/c, ToF-ERDA, and HR-PIXE," *Materials (Basel).*, vol. 10, no. 12, p. 1041, 2017.

[39] G. Schiwietz, E. Luderer, G. Xiao, and P. Grande, "Energy dissipation of fast heavy ions in matter," *Nucl. Instruments Methods Phys. Res. Sect. B Beam Interact. with Mater. Atoms*, vol. 175, pp. 1–11, 2001.

[40] R. Spohr, "Status of ion track technology — Prospects of single tracks," *Radiat. Meas.*, vol. 40, pp. 191–202, 2005.

[41] R. L. Fleischer, P. B. Price, and R. M. Walker, "Ion explosion spike mechanism for formation of charged particle tracks in solids," *J. Appl. Phys.*, vol. 36, no. 11, pp. 3645–3652, 1965.

[42] N. Itoh and A. M. Stoneham, *Materials Modification by Electronic Excitation*. Cambridge: Cambridge University Press, 2003.

[43] C. Dufour, A. Audouard, F. Beuneu, J. Dural, J. P. Girard, A. Hairie, M. Levalois, E. Paumier, and M. Toulemonde, "A high-resistivity phase induced by swift heavy-ion irradiation of bi: a probe for thermal spike damage," *J. Phys. Condens. Matter*, vol. 5, no. 26, pp. 4573–4584, 1993.

[44] A. Colder, O. Marty, B. Canut, M. Levalois, P. Marie, X. Portier, and S. Ramos, "Latent track formation in GaAs irradiated with 20, 30, and 40 mev fullerenes," *J. Appl. Phys.*, vol. 91, no. 9, pp. 5853–5857, 2002.

[45] H. Harima, "Raman studies on spintronics materials based on wide bandgap semiconductors," *J. Phys. Condens. Matter*, vol. 16, no. 48, pp. 5653–5660, 2004.

[46] E. De Luca, R. Sanatinia, S. Anand, and M. Swillo, "Focused ion beam milling of gallium phosphide nanostructures for photonic applications," *Opt. Mater. Express*, vol. 6, no. 2, pp. 587–596, 2016.

[47] J. Václavík and D. Vápenka, "Gallium Phosphide as a material for visible and infrared optics," *EPJ Web Conf.*, vol. 28, pp. 1–4, 2013.

[48] GSI, "Linear Accelerator UNILAC." [Online]. Available: https://www.gsi.de/en/researchaccelerators/accelerator_facility/linear_accelerator.htm.

[49] HZDR Dresden, "High Energy Ion Accelerator." [Online]. Available: https://www.hzdr.de/db/Cms?pOid=41230&pNid=0.

[50] F. Grossmann, R. Heller, M. Kreller, U. Kentsch, S. Landgraf, V. P. Ovsyannikov, M. Schmidt, F. Ullman, and G. Zschornack, "Production of highly charged ions in

the range of energy of 10 V · q up to MeV," *Nucl. Instruments Methods Phys. Res. Sect. B Beam Interact. with Mater. Atoms*, vol. 256, no. 1, pp. 565–570, 2007.

[51] V. P. Ovsyannikov and G. Zschornack, "First investigations of a warm electron beam ion trap for the production of highly charged ions," *Rev. Sci. Instrum.*, vol. 70, no. 6, pp. 2646–2651, 1999.

[52] P. J. de Pablo, "Introduction to Atomic Force Microscopy," in *Single Molecule Analysis Method and Protocols*, E. J. Peterman and G. J. Wuite, Eds. Amsterdam: Humana Press, 2011, pp. 197–212.

[53] D. Schwen, "Structural and electronic properties of swift heavy ion tracks in amorphous carbon," Georg-August-Universitat zu Gottingen, Germany, 2007.

[54] I. Horcas, R. Fernández, J. M. Gómez-Rodríguez, J. Colchero, J. Gómez-Herrero, and A. M. Baro, "WSXM: A software for scanning probe microscopy and a tool for nanotechnology," *Rev. Sci. Instrum.*, vol. 78, no. 1, pp. 1–8, 2007.

[55] D. Necas and P. Klapetek, "Gwyddion : an open-source software for SPM data analysis," *Cent. Eur. J. Phys.*, vol. 10, no. 1, pp. 181–188, 2012.

[56] M. Nastasi, J. W. Mayer, and Y. Wang, *Ion Beam Analysis: Fundamentals and Applications*. New York: CRC Press, 2014.

[57] B. Schmidt and W. Wetzig, *Ion Beams in Materials Processing and Analysis*. Wien: Springer, 2013.

[58] W. Wesch, *Ion Beam Modification of Solids*, Springer S. Switzerland: Springer, 2016.

[59] J. Yang and M. R. Alexander, "Techniques for analysing biomaterial surface chemistry," in *Surface Modification of Biomaterials*, R. Williams, Ed. Cambridge: Woodhead Publishing Limited, pp. 205–232, 2011.

[60] R. L. Dubey, S. K. Dubey, A. D. Yadav, and D. Kanjilal, "Swift Heavy Ion Induced Nanohill Formation on the Surface of GaP," *Int. J. Nanosci.*, vol. 10, no. 1, pp. 105–109, 2011.

[61] W. Wesch, A. Kamarou, E. Wendler, and S. Klaumu, "593 MeV Au irradiation of InP , GaP , GaAs and AlAs," *Nucl. Instruments Methods Phys. Res. Sect. B Beam Interact. with Mater. Atoms*, vol. 242, pp. 363–366, 2006.

[62] C. Cotirlan, C. Logofatu, C. C. Negrila, R. V. Ghita, A. S. Manea, and M. F. Lazarescu, "XPS analysis of n-GaP(111) native and etched surfaces," *J. Optoelectron. Adv. Mater.*, vol. 11, no. 4, pp. 386–390, 2009.

[63] J. R. Ferraro and K. and Krishanan, *Practical Fourier Transform Infrared Spectroscopy*. San Diego: Academic Publisher Inc, 1990.

[64] P. Sharma, "Electrical conductivity of ion irradiated Ge20Se80−xBix thin films,"

Radiat. Meas., vol. 36, no. 1–6, pp. 663–666, 2003.

[65] M. Varshney, A. Sharma, and H. J. Shin, "Swift Heavy Ion-Irradiation Effects on Structural , Optical and Magnetic Properties of CeO 2 Thin Films," *Adv. Sci. Eng. Med.*, vol. 7, no. 3, pp. 1–7, 2015.

[66] R. Dalven, "Empirical relation between energy gap and lattice constant in cubic semiconductors," *Phys. Rev. B*, vol. 8, no. 12, pp. 6033–6034, 1973.

[67] A. Benyagoub, "Mechanism of the monoclinic-to-tetragonal phase transition induced in zirconia and hafnia by swift heavy ions," *Phys. Rev. B*, vol. 72, no. 9, p. 94114, 2005.

[68] M. Toulemonde, A. Benyagoub, C. Trautmann, N. Khalfaoui, M. Boccanfuso, C. Dufour, F. Gourbilleau, J. J. Grob, J. P. Stoquert, J. M. Costantini, F. Haas, E. Jacquet, K. Voss, and A. Meftah, "Dense and nanometric electronic excitations induced by swift heavy ions in an ionic CaF 2 crystal : Evidence for two thresholds of damage creation," *Phys. Rev. B*, vol. 85, no. 5, p. 54112, 2012.

Vitae

Personal Data

Name : Zamzam Ibnu Sina

Nationality : Indonesian

Date of Birth : 12 November 1990

Email : zamzam.itb@gmail.com

Address : Jl Teknologi V no.6 Cimindi Raya, Cimahi, Indonesia, 40513

Academic Background

2015 - 2018 MSc in Physics, King Fahd University of Petroleum and Minerals, Dhahran, Saudi Arabia

Thesis: Ion-Induced Modifications in Gallium Phosphide Single Crystals

2008-2013 BSc in Physics, Institut Teknologi Bandung (ITB), Bandung, Indonesia

Thesis: Finite Difference Time Domain (FDTD) Study of Localized Surface Plasmon Effect of Metallic Nanosphere

Presented in International Symposium in Modern Optics and its Applications (ISMOA), 2013